Strathprints Institutional Repository

Asteroid Rotation and Orbit Control via Laser Ablation

Massimo Vetrisano[1], Camilla Colombo[2], Massimiliano Vasile[1]

[1] *Department of Mechanical and Aerospace Engineering, University of Strathclyde, G1 1XQ Glasgow, UK; massimo.vetrisano@strath.ac.uk, massimiliano.vasile@strath.ac.uk*

[2] *Department of Aerospace Science and Technology, Politecnico di Milano,* 20156 *Milano, Italy; Astronautics group, University of Southampton, SO17 1BJ Southampton, UK c.colombo@soton.ac.uk*

This paper presents an approach to control the rotational motion of an asteroid while a spacecraft is deflecting its trajectory through laser ablation. During the deflection, the proximity motion of the spacecraft is coupled with the orbital and rotational motion of the asteroid. The combination of the deflection acceleration, solar radiation pressure, gravity field and plume impingement will force the spacecraft to drift away from the asteroid. In turn, a variation of the motion of the spacecraft produces a change in the modulus and direction of the deflection action which modifies the rotational and orbital motion of the asteroid. An on-board state estimation and control algorithm is then presented that simultaneously provides an optimal proximity control and a control of the rotational motion of the asteroid. It will be shown that the simulataneous control of the rotational and proximity motions of asteroid and spacecraft has a significant impact on the required deflection time.

Keywords

Asteroid rotation control; asteroid deflection; proximity operation; spacecraft control; rotational dynamics.

1   Introduction

Near Earth objects (NEOs) have been generating a growing scientific interest because, as primordial remnants of our solar system, they preserve precious information on its formation, composition and evolution. Besides, their collision with the early Earth would have influenced the shape and composition of our planet. Some NEOs are especially attractive targets for low-cost missions, because of their orbital accessibility with current technologies. This easy accessibility suggests the possibility to use them as source of raw materials and for the settlement of future human outposts (Seboldt et al., 2000). At the same time, NEO collisions with the Earth represent a possible threat to mankind. In particular, small size asteroids pose a concrete threat on the short term, with significant expected damages at regional level. Advances in orbit determination and theoretical studies on hazard characterisation have increased the capability of predicting potential impacts (Chapman et al., 1994). The manipulation of asteroid, instead, still remains an open problem. Increasing our capabilities in asteroid orbit and attitude manipulation is therefore required, both for reducing the collision hazard and for future asteroid exploitation.

In the past two decades, different techniques for asteroid manipulation have been studied and compared; among them, surface ablation was shown to be theoretically one of the most promising methods (Sanchez et al., 2009). Ablation is achieved by irradiating the asteroid with a high intensity light source. Within the illuminated spot area, the absorbed energy increases the temperature of the asteroid, enabling it to

sublimate. The ablated material then expands to form an ejecta plume. The resulting thrust induced by the ejecta plume pushes the asteroid away from its original trajectory.

In a recent study, supported by the European Space Agency (ESA), the Light Touch[2] concept was proposed as technology demonstrator to validate this concept (Vasile et al., 2013). The main specifications of this study were to impart a minimum variation of velocity of 1 m/s over the course of one year operations to a small asteroid 2-4 meters in diameter or equivalently 130 tons in mass, considering an average density of a silicate asteroid. Further constraints limited the target asteroid's orbital elements to have a perihelion larger than 0.7 AU, an aphelion smaller than 1.4 AU and an inclination smaller than 5 degrees. Light Touch[2] employs a laser beam, focused on the surface of the asteroid, to generate a controllable thrust via surface ablation.

This paper presents an approach to control the rotational motion of an asteroid, while the spacecraft deflects the asteroid's trajectory through laser ablation.

During the deflection, the proximity motion of the spacecraft is coupled with the orbital and rotational motion of the asteroid. In fact, a change in the angular velocity of the asteroid induces a variation of the ablation rate that, in turns, affects both the orbital and rotational motion of the asteroid. At the same time a change in the ablation rate, orbital and rotational motion affects the proximity motion of the spacecraft as it changes the perturbations due to the impingement with the plume of gas, the gravity of the asteroid and the relative acceleration between asteroid and spacecraft. Since the spot size of the laser beam needs to be kept below an acceptable limit to guarantee constant ablation, the spacecraft needs to manoeuvre to maintain its relative distance under the effect of perturbations that are a function of the ablation process. Since, as shown in the works of Kahle et al., 2005 and Colombo et al., 2006, the lower is the angular velocity of the asteroid the higher is the imparted deflection acceleration, the simultaneous control of both the spacecraft relative position and asteroid's angular velocity is paramount.

The asteroid is modelled as a tumbling ellipsoid with a random initial angular velocity vector and the characteristics of the reference asteroid used in the Light Touch[2] study. The rotational motion of the asteroid is then controlled by off-setting the thrust vector, induced by the laser, with respect to the centre of mass. The spacecraft proximity motion and the instantaneous rotational velocity of the asteroid are estimated through two filters: an augmented Unscented Kalman Filter that determines the spacecraft trajectory from optical and laser ranging measurements, and a batch filter which processes optical flow measurements from the camera to reconstruct the rotational velocity of the asteroid.

It will be shown that, through the proposed control method, the time required to achieve a given variation of velocity can be substantially decreased and the displacement of the asteroid from its nominal unperturbed orbit maximised.

This paper is organised as follows. Section 2 briefly introduces the thrust and contamination models. Then, Section 3 describes the spacecraft dynamics and control during proximity operations. Section 4 presents the asteroid rotational dynamics and the control to decrease the angular velocity. Section 5 focuses on the proximity and rotational motion reconstruction. Finally, Section 6 shows some results for the proposed mission scenario.

2 Ablation Model

This section outlines the ablation model used to predict the torque and force acting on the asteroid and the spacecraft. A more complete description, including some experimental results can be found in Vasile et al., 2014; Vasile et al., 2013; Vasile et al., 2013b; Gibbings et al., 2013.

The force acting on the asteroid F_L is given by the product of the velocity of the ejected gas $\bar{v}$ and the mass flow rate of the ablated material $\dot{m}$:

$$F_L = \lambda \bar{v} \dot{m} \tag{1}$$

where $\lambda = 0.88$ is a constant scatter factor used to account for the non-unidirectional expansion of the ejecta. The mass flow rate is given by the integral, over the area illuminated by the laser where ablation occurs, of the mass flow rate per unit area $\dot{\mu}$:

$$\dot{m} = 2V_{rot} \int_{0}^{y_{max}} \int_{t_{in}}^{t_{out}} \dot{\mu} \, dt \, dy \tag{2}$$

where V_{rot} is the speed at which the surface of the asteroid is moving under the spotlight, y_{max} is the maximum width of the spot. The time t_{in} identifies the point under the spotlight at which the ablation starts while t_{out} is the time at which a point of the surface moving with velocity V_{rot} exits from the spotlight. The assumptions are that locally the surface is flat and the spot is a circle, and that the temperature of a point under the spot light progressively increases but with negligible or no vaporisation till time t_{in}. In this case, an approximated solution for the temperature T after an exposure time t can be derived assuming that radiation loss Q_{rad} is small compared to the absorbed laser power per unit area P_{in} (see Anisimov et al. 1995) and is given by:

$$T = \frac{2P_{in}}{\pi \kappa_A} \sqrt{\frac{\kappa_A t}{C_v \rho_A}} \tag{3}$$

From which one can estimate t_{in} as:

$$t_{in} = \frac{\pi^2}{4} \left(\frac{\sqrt{C_v \kappa_A \rho_A} T_S}{P_{in}} \right)^2 \tag{4}$$

The mass flow rate $\dot{\mu}$ per unit area is expressed as:

$$E_v^* \dot{\mu} = P_{in} - Q_{RAD} - Q_{COND} \tag{5}$$

where E_v^* is an augmented enthalpy of complete vaporisation, Q_{COND} the conduction and Q_{RAD} the radiation loss per unit area. The augmented enthalpy $E_v^* = E_v^*(T_0, T_S, C_p, C_v, \bar{v})$ depends on the initial surface temperature T_0, the vaporisation temperature T_S (computed for each laser intensity), the heat capacity of solid phase C_v, vapour phase C_p and the mean ejection velocity $\bar{v}$. Note that the model used in this paper considers a conservative simplification of the ablation process. A more rigorous derivation can be found in Thiry and Vasile 2014 and Thiry and Vasile 2015 which provides higher values of the achievable thrust. However, in this paper we maintain all the conservative assumptions of the model reported in Vasile et al.

2014 and Gibbings et al. 2013 to account for additional unmodelled effects like the actual orography, surface and material inhomogeneity and porosity.

The absorbed laser power per unit area P_{in} in Eq. (5) is computed assuming that the beam is generated by an electrically pumped laser. The electric power is generated by a solar array with conversion efficiency η_s. The electric power is then converted into laser power with efficiency η_L. The surface of the asteroid is absorbing only the fraction $\alpha_M = (1 - \alpha_s)$ of the incoming light, where α_s is the albedo at the frequency of the laser light. One can consider this as the worst case scenario. The absorbed power per square meter at the spot is therefore:

$$P_{in} = \tau \alpha_M \eta_P \eta_L \eta_s \frac{P_{1AU} A_{SA}}{A_{spot} r_{AU}^2}$$
(6)

where τ is a degradation factor due to contamination, η_P is the efficiency of the power system, P_{1AU} is the solar constant at 1 Astronomical Unit (AU), A_{SA} is the area of the solar arrays, A_{spot} is the area of the spot and r_{AU} is the distance from the Sun measured in AU. The degradation factor can be computed by following the experimental results in Gibbings et al. 2013 and taking the plume density $\rho_{plume}(r,\xi)$ at any given distance r from the spot location, and elevation angle ξ from the surface normal. The ejecta thickness on any exposed surface, h, grows linearly with the mean ejection velocity at the asteroid surface $\bar{v}$ and the plume density $\rho_{plume}(r,\xi)$, which decreases as the distance from the asteroid increases. The increasing thickness of the contaminants will ultimately reduce the power generated by the solar arrays and, therefore, the laser output power. The consequence is a reduction of the thrust imparted onto the asteroid until ablation ceases completely and the thrust with it. The reduction of the power generated by the solar arrays, τ, can be computed from the Beer-Lambert-Bougier law:

$$\tau = e^{-\eta h}$$
(7)

where η is the absorbance per unit length of the accumulated ejecta. Table 1 reports the parameters used for the calculation of Eq. (1) to (7). Note that the density of the material used in the laser model is higher than the average density of the asteroid, to remain consistent with Gibbings et al. 2013, which results in slightly higher heat conduction and a lower thrust magnitude.

2.1 Optimal distance from the asteroid and force due to the ablation

The asteroid's orbital velocity variation given by the ablation process can be computed as:

$$\delta v_I = \int_{start\ ablation}^{stop\ ablation} \frac{F_L(t)}{m_a(t)} dt$$
(8)

where m_a is the mass of the asteroid which is decreasing due to the ablation process. From the ablation model presented in the previous section one can see that the thrust F_L is a function of both the power input to the laser and the distance from the spot, as the contamination of the solar arrays depends on the mass flow rate. Figure 1 represents the contour line of the thrusting time, in days, required to achieve a δv_I of 1 m/s with the laser positioned at a distance of 50 meters from an S-class asteroid with a mean radius of 2.18 m, a spinning rate of 19.47 rotations per hour and a mass of 130 000 kg. The thrusting time is plotted against the power input to the laser and the radius of the laser spot.

Table 1. Laser system coefficients and ablation parameters.

	Parameter	Value
Albedo at the frequency of the laser	α_s	0.16
Efficiency of the power system	η_P	0.85
Efficiency of the laser	η_L	0.55
Efficiency of the solar arrays	η_S	0.3
Absorbance per unit length	η	$2 \cdot 10^{-4} cm^{-1}$
Heat capacity of the solid phase	C_v	1361 J/(K·kg)
Heat capacity of the vapour phase	C_p	1350 J/(K·kg)
Conductivity	κ_A	4.51 W/(m·K)
Mean density of the asteroid	ρ_A	3500 kg/m^3

Figure 1 shows that a variation of 38% in the radius of the spot corresponds to an increase in the deflection time between 140 and 180 days. A variation of the radius of the spot corresponds to the defocusing of the beam and is due to two reasons: the excavation of a groove along the surface of the asteroid and the variation of the relative position of the spot from the laser source due to the rotation of the asteroid and the relative motion of the spacecraft. The distance from the focal point, along the beam, at which the beam radius is $w_0 \sqrt{2}$ (known as Rayleigh length, $l_{Rayleigh}$, Siegaman 1986), with w_0 the radius at the focal point, is about 3 m, assuming a 50 mm in diameter focusing mirror, at a nominal distance of 50 m from the laser source to the spot. With reference to Figure 1, if the nominal radius is 0.8 mm at 3 m from the focal point the beam radius would be 1.13 mm. This means that at the rate of 19.47 rotations per hour, with the current model, a fluctuation of the distance within the Rayleigh length would yield a variation of about 60% of the deflection time. It follows that the Rayleigh length can be used to derive a requirement on the control of the distance between the spacecraft and the surface of the asteroid, which can be converted in a requirement on the control of the distance between the spacecraft and the asteroid centre of mass as it will be illustrated in Section 3.1.
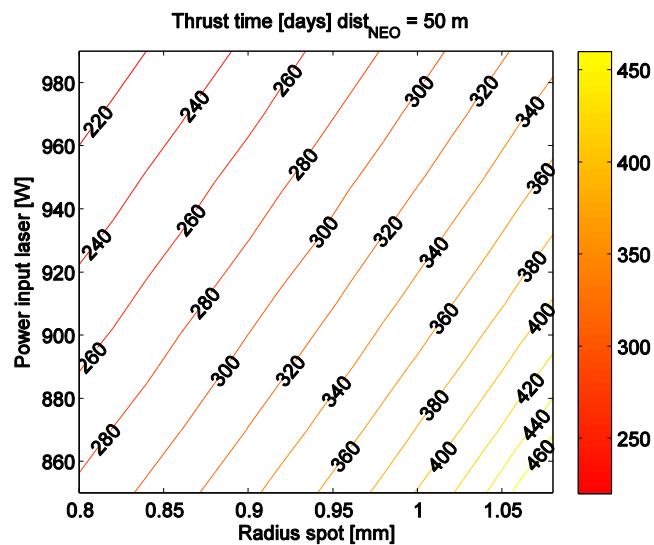
Figure 1. Thrusting time, in days, required to achieve 1 m/s velocity change with a shooting distance of 50 m.

The variation of the deflection time with the defocusing of the beam is however a function of the rotation rate. In fact, if one assumes a constant input power of 860 W, a nominal spot size of 0.8 mm (Vasile et al., 2013), and an optics designed to focus the beam at a nominal distance of 50 m from the laser source, a variation of the distance will produce a bigger cross section A_{spot} of radius w on the surface of the asteroid consistently with the Rayleigh length, as shown in the following equation:

$$w(l) = w_0 \frac{\sqrt{2}(l - l_{focusing})}{l_{Rayleigh}}$$

$$A_{spot} = \pi w^2 = 2\pi w_0^2 \frac{(l - l_{focusing})^2}{l_{Rayleigh}^2}$$

(9)

where l is the distance from the spot, $l_{focusing}$ is the focusing length. This means that the light intensity at the spot decreases as the distance of the laser source from the surface departs from the focusing distance. Furthermore, Eqs (2) and (6) give a mass flow that decreases if the surface under the laser moves faster. Therefore, if one assumes a flat surface moving with velocity V_{rot} transversally to the incident light and positioned at a distance l from the laser source the resulting thrust is the one represented in Figure 2.

As one can see, the force increases as the velocity V_{rot} decreases and an absolute maximum is reached when V_{rot} is zero and the distance equals the focusing length. Moreover, for higher values of velocity, moving by 3 m with respect to the focusing length causes a reduction of about 75% of the nominal value. With reference to Figure 2b, the trend is almost linear in the distance although a curvature can be seen. For lower velocities, the variation of the force with the distance is less pronounced, because the surface resides under the laser for longer time. Note that the results in Figure 2 and in Figure 1 depend on the laser intensity and on the material properties. Hence, different exact control requirements would be derived for different lasers, material properties but also for a more accurate modelling of the ablation process.
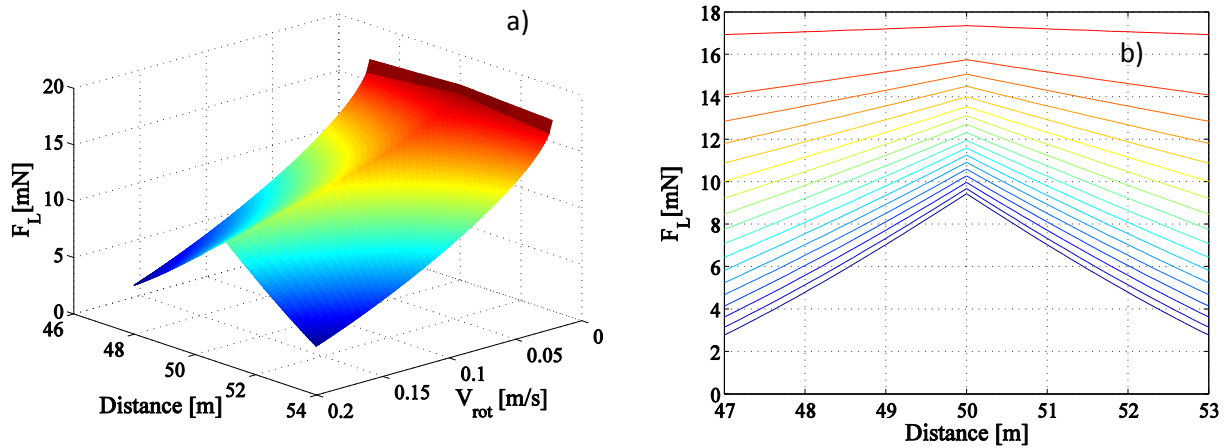
Figure 2. a) Force due to the ablation process with respect to the laser distance from the spot and the velocity of the surface under the spot light; b) contour plot showing the force trend with respect to the distance at increasing tangential velocity.

If the incident laser beam is not perpendicular to the surface the spot deforms from a circle to an ellipse and its area increases. The travel time of a point under the spot light t_{out}-t_{in} then changes depending on the direction of the velocity V_{rot} with respect to the local normal and Eq.(2) needs to be modified to account of

the actual geometry. In this paper a simpler and more conservative approach is taken. Instead of calculating the exact travelling time the light intensity is simply reduced by modifying Eq. (9) as follows:

$$A_{spot} = 2\pi w_0^2 \frac{(I - I_{focusing})^2}{I_{Rayleigh}^2} \frac{1}{\cos\theta_{laser-normal}} \tag{10}$$

where $\theta_{laser-normal}$ is the angle between the incident laser beam and local normal. The area given by Eq. (10) is then used in both Eq. (2) and (6). As one can see as the cross section increases with this angle, the power density decreases and progressively reduces to zero for nearly tangential configurations.

3   Proximity Motion Dynamics and Control

During the ablation process the spacecraft flies in close formation with the asteroid, thus it is convenient to describe the motion of the spacecraft in the rotating Hill reference frame. In the proximity of the asteroid, the spacecraft is subject to the force due to solar radiation pressure, the gravity of the asteroid, the gravity of the Sun, the centrifugal and Coriolis forces, the recoil of the laser, and the force induced by the impingement with the plume. Moreover, the asteroid is accelerating under the effect of laser ablation, and, thus, the spacecraft experiences the same acceleration in magnitude but in the opposite direction.

The asteroid's orbit around the Sun is defined with respect to the Sun-centred equatorial inertial reference frame $\mathbf{I}-\mathbf{J}-\mathbf{K}$ as shown in Figure 3a. In this work, it is assumed that the asteroid is an ellipsoid with semi-axes a_I, b_I, c_I defined in the body fixed reference frame $\bar{\mathbf{i}}-\bar{\mathbf{j}}-\bar{\mathbf{k}}$ (principal axes of inertia) as shown Figure 3b.
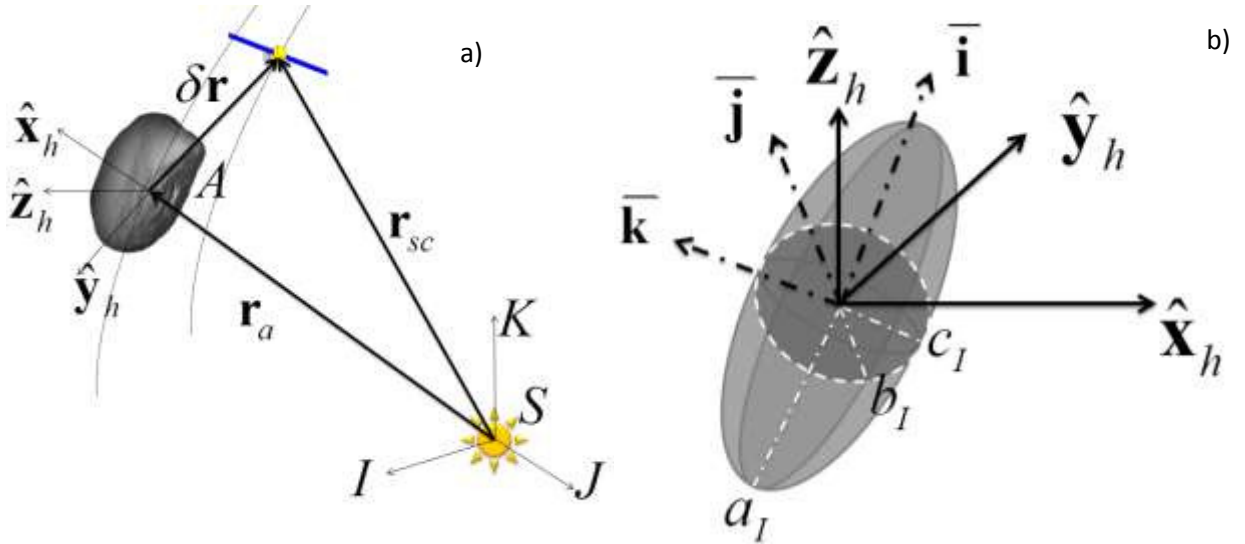
Figure 3. (a) Definition of the inertial and Hill's reference frames; (b) definition of the asteroid's body fixed reference frame.

With reference to Figure 3a, $\delta\mathbf{r}$ is the position vector of the spacecraft with respect to the asteroid, $\mathbf{r}_a$ and $\mathbf{r}_{sc}$ are respectively the position of the asteroid and the spacecraft in the inertial frame. The spacecraft state vector relative to the asteroid is defined as $[\delta\mathbf{r}^h, \delta\dot{\mathbf{r}}^h]^T = [x_h, y_h, z_h, v_{x_h}, v_{y_h}, v_{z_h}]^T$ in the Hill reference frame.

The gravity field of the asteroid is expressed as the sum of a spherical field plus a second-degree and second-order field (Hu, 2002):

$$U_{20+22}(\delta \mathbf{r}_b) = \frac{\mu_A}{\delta r^3}\left(C_{20}(1-\frac{3}{2}\cos^2\gamma)+3C_{22}\cos^2\gamma\cos 2\psi\right)$$ (11)

where the harmonic coefficients C_{20} and C_{22} are a function of the semi-axes:

$$C_{20} = -\frac{1}{10}(2c_l^2 - a_l^2 - b_l^2)$$
$$C_{22} = \frac{1}{20}(a_l^2 - b_l^2)$$ (12)

and μ_a is the gravitational constant of the asteroid. The angles γ and ψ are defined as

$$\gamma = \arctan\left(\frac{z_b}{\sqrt{x_b^2 + y_b^2}}\right)$$
$$\psi = \arctan\left(\frac{y_b}{x_b}\right)$$ (13)

where the subscript b refers to the position of the spacecraft in the body fixed reference frame. The motion of the spacecraft in the proximity of the asteroid is governed by the following set of equations:

$$\delta\ddot{\mathbf{r}}^h = -\ddot{\mathbf{r}}_a^h - 2\dot{\boldsymbol{\theta}}^h\times\delta\dot{\mathbf{r}}^h - \dot{\boldsymbol{\theta}}^h\times\delta\mathbf{r}^h - \dot{\boldsymbol{\theta}}^h\times(\dot{\boldsymbol{\theta}}^h\times\delta\mathbf{r}^h) - \frac{\mu_{sun}}{r_{Sc}^3}(\delta\mathbf{r}^h + \mathbf{r}_a^h) - \frac{\mu_a}{\delta r^3}\delta\mathbf{r}^h + \nabla U + \frac{\mathbf{F}_{Sc}(\delta\mathbf{r}^h, \mathbf{r}_a^h)}{m_{sc}} =$$

$$= -\ddot{\mathbf{r}}_{a-g}^h - 2\dot{\boldsymbol{\theta}}^h\times\delta\dot{\mathbf{r}}^h - \dot{\boldsymbol{\theta}}^h\times\delta\mathbf{r}^h - \dot{\boldsymbol{\theta}}^h\times(\dot{\boldsymbol{\theta}}^h\times\delta\mathbf{r}^h) - \frac{\mu_{sun}}{r_{Sc}^3}(\delta\mathbf{r}^h + \mathbf{r}_a^h) + \mathbf{a}_p$$ (14)

where the superscript h refers to the projection onto the Hill's local axes. The force vector $\mathbf{F}_{sc}(\delta\mathbf{r}^h, \mathbf{r}_a^h)$ is defined below in Eq.(18). The acceleration $\ddot{\mathbf{r}}_a$, which the asteroid is subjected to, in the inertial frame is defined as:

$$\ddot{\mathbf{r}}_a = -\frac{\mu_{sun}}{r_a^3}\mathbf{r}_a - \frac{\mu_{Sc}}{\delta r^3}\delta\mathbf{r} + \mathbf{a}_L = \ddot{\mathbf{r}}_{a-g} + \mathbf{a}_L$$ (15)

$\ddot{\mathbf{r}}_{a-g}$ represents the dynamics of the asteroid trajectory under gravitational effects only. The second component on the right hand side of Eq. (15) represents the tugging effect exerted by the spacecraft on the asteroid, and $\mathbf{a}_L = \mathbf{F}_L/m_a$ is the acceleration due to the laser ablation process (see Section 2). Note we did not consider the solar radiation pressure acting on the asteroid because its area to mass ratio is almost two orders of magnitude smaller than the spacecraft one. This differential acceleration is well within the system noise we included in our simulations.

The quantity $\dot{\boldsymbol{\theta}}$ of Eq. (14) is the angular velocity with which the reference frame rotates. In the local reference frame the variation of $\dot{\boldsymbol{\theta}}$ can be derived from:

$$\mathbf{r}_a^h\times(\ddot{\boldsymbol{\theta}}^h\times\mathbf{r}_a^h)+2\mathbf{r}_a^h\times(\dot{\boldsymbol{\theta}}^h\times\mathbf{r}_a^h)=\mathbf{r}_a^h\times\mathbf{a}_L^h$$ (16)

being $\mathbf{a}_L^h$ the projection of $\mathbf{a}_L$ onto the Hill's reference frame. Eq. (16) states that the instantaneous variation of the angular momentum with respect to time is proportional to the induced deflection acceleration $\mathbf{a}_L$. The acceleration $\mathbf{a}_p$ comprises all the perturbative accelerations acting on the spacecraft as shown in Eq.(17):

$$\mathbf{a}_p = -\mathbf{a}_L^h + \frac{\mathbf{F}_{sc}(\delta \mathbf{r}^h, \mathbf{r}_a^h)}{m_{sc}} - \frac{\mu_a}{\delta r^3} \delta \mathbf{r}^h + \nabla U \tag{17}$$

The force vector $\mathbf{F}_{sc}(\delta \mathbf{r}^h, \mathbf{r}_a^h)$ includes all the perturbations due to solar radiation pressure, the laser recoil and plume impingement (Vasile et al., 2013):

$$\mathbf{F}_{Solar}(\delta \mathbf{r}^h, \mathbf{r}_a^h) = C_R S_{srp} \left(\frac{r_{AU}}{r_{sc}} \right)^2 A_M \frac{(\delta \mathbf{r}^h + \mathbf{r}_a^h)}{r_{Sc}}$$

$$\mathbf{F}_{recoil}(\delta \mathbf{r}^h, \mathbf{r}_a^h) = \eta_{sys} S_{srp} \left(\frac{r_{AU}}{r_{sc}} \right)^2 A_{SA} \frac{\delta \mathbf{r}^h}{\delta r} \tag{18}$$

$$\mathbf{F}_{plume}(\delta \mathbf{r}^h) = \rho_{plume}(\delta r) \bar{v}_{plume}^2(\delta r) A_{eq} \frac{\delta \mathbf{r}^h}{\delta r}$$

where C_R is the reflectivity coefficient and S_{srp} is the solar radiation pressure at 1 AU, $\eta_{sys} = \tau \alpha_M \eta_P \eta_L \eta_S$ is the system efficiency, A_M is the area of the solar arrays plus the area of spacecraft bus, A_{eq} is the spacecraft cross section area facing the incoming plume of gas, ρ_{plume} and $\bar{v}_{plume}$ are respectively the plume's density and velocity.

3.1 Proximity Control Strategy

In section 2.1 it was suggested that the Rayleigh length could be used to derive a requirement on the relative distance between laser head and asteroid's surface. If one considers a V_{rot} equal or lower than 19.47 rotations per hour (see Section 2.1), then a Rayleigh length of up to 3 m can be deemed to be acceptable without any control of the relative position. On the other hand, in order to control the rotational motion of the asteroid the laser needs to hit different points on its surface while the asteroid is rotating. It is therefore necessary to ensure that the difference between the focal distance and the distance between the laser head and the surface remains within the Rayleigh length at all times.

Let us consider the asteroid to be an ellipsoid with semi-axes $a_l = 3\,\text{m}$, $b_l = 2.3\,\text{m}$ and $c_l = 1.5\,\text{m}$, with b_l the spinning axis, and the spacecraft located at a constant distance of 50 m from the asteroid's Centre of Mass (CoM) in the plane perpendicular to b_l. Furthermore, let us assume that the focal distance is 49.3 m from the laser head. With reference to Figure 4a, the difference between the focusing length and the distance between the laser head and the surface of the asteroid can now be calculated for each visible (i.e. reachable from the laser) point on the surface and for rotation angles.

If the modulus of this difference was greater than the Rayleigh distance, then the yield of the ablation process would be compromised and might even cease. Figure 4b shows the maximum difference between the range to surface and the focusing length for different rotation angles first around $\hat{\mathbf{x}}_h$ and then $\hat{\mathbf{z}}_h$. Given the symmetry of the problem, only rotation angles from -90 to 90 degrees were considered. The discontinuity at about ± 25 degrees and ±86 degrees is due to the fact that the maximum variation goes

from surface points closer to the spacecraft to points located farther from it. The maximum variation is reached at 0 degrees when the major axis is aligned with the asteroid-spacecraft direction and at ±35 degrees when the range to surface is maximum. We can see that the maximum difference between the range to a surface point and the focusing length is about 2.3 m.
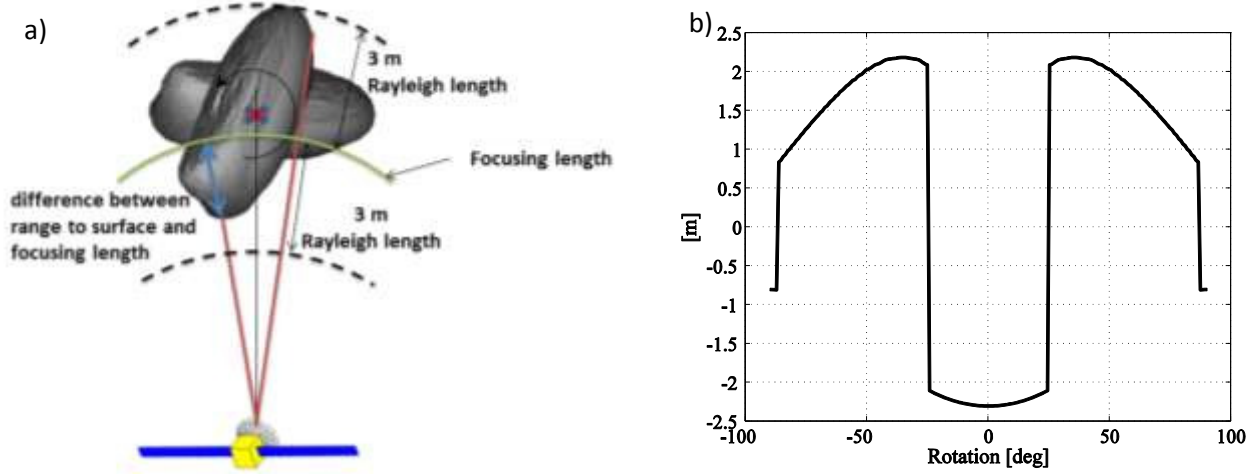
Figure 4. a) Difference between range to a surface point and the focusing length with Rayleigh length b) Maximum difference as a function of the asteroid rotation around b_l (spacecraft positioned at 50 m from the asteroid's CoM and focusing length of 49.3 m).

Given the maximum acceptable excursion of 3 m defined by the Rayleigh length, the spacecraft needs to be maintained within a 0.7 m radius control sphere around its nominal position with respect to the centre of mass of the asteroid. Nonetheless in order to compensate estimation errors and maintain the variations of the thrust due to the defocussing and $\theta_{laser-normal}$ contained and maintain the laser at optimal operative conditions, we decided to activate the control logics for a 0.4 m control sphere. In the following, it is assumed that the nominal position is placed at $y_h = -50$ m with respect to the asteroid centre of mass.

If $\mathbf{d} = [d_1, d_2, d_3]^T$ is the displacement from the nominal position in the Hill's reference frame, a correction manoeuvre $\Delta\mathbf{v}$ is then implemented when $\|\mathbf{d}\| = d^e/2$, where d^e is the diameter of the sphere.

In the derivation of the control, it is assumed that the acceleration $\mathbf{a}_p$ acting on the spacecraft is constant within the control sphere. Under this assumption, the magnitude of each component Δv_i of the correction manoeuvre can be derived from the evolution of the displacement d_i in a time interval Δt. If d_i^s is the value of the displacement component when the spacecraft touches the limits of the control sphere and v_i^s the corresponding velocity component, then the displacement after an interval Δt from the implementation of the control manoeuvre is:

$$d_i = d_i^s + (v_i^s + \Delta v_i)\Delta t + a_{p,i}\frac{\Delta t^2}{2} \tag{19}$$

where $a_{p,i}$ is the i-th component of the acceleration $\mathbf{a}_p$ at the time the correction is performed. The control impulse bit Δv_i can now be allocated such that the spacecraft reaches a displacement $d_i = -d_i^s$ with the corresponding velocity equal to zero. The time Δt_c to reach this condition is:

$$\left(v_i^s + \Delta v_i\right) + a_{p,i}\Delta t_c = 0 \Rightarrow \Delta t_c = -\frac{v_i^s + \Delta v_i}{a_{p,i}} \tag{20}$$

By substituting Δt_c into Eq. (19), one obtains the value of the i-th component of the correction manoeuvre:

$$\Delta v_i^2 + 2v_i^s \Delta v_i + \left(v_i^s\right)^2 + 2a_{p,i}d_i^s = 0 \tag{21}$$

Eq. (21) has two roots, one of which produces a positive value of Δt_c. Section 5 will present the navigation strategy to estimate the displacement d_i^s, velocity v_i^s and disturbing acceleration $\mathbf{a}_p$.

4 Asteroid Rotational Dynamics and Control

From Figure 2 one can see that the ablation force is higher when the velocity V_{rot} is lower because the time interval $[t_{in}\ t_{out}]$ to sublimate the surface tends to infinity. The velocity V_{rot} is given by the modulus of the cross product of the istantaneous angular velocity and $\mathbf{s}$, the position vector of the spot on the surface of the asteroid, with components $\mathbf{s} = [s_x^b \quad s_y^b \quad s_z^b]^T$ in the body frame:

$$V_{rot} = \|\boldsymbol{\omega} \times \mathbf{s}\|$$

This means that decreasing the asteroid's angular velocity can increase the yield of the ablation process.

The asteroid's rotational motion is governed by the following system of differential equations:

$$\dot{\mathbf{q}} = \frac{1}{2}\boldsymbol{\Pi}\mathbf{q}$$
$$\mathbf{I}\dot{\boldsymbol{\omega}} + \boldsymbol{\omega} \times \mathbf{I}\boldsymbol{\omega} = \mathbf{M}_c \tag{22}$$

where $\mathbf{q} = [q_1 \quad q_2 \quad q_3 \quad q_4]^T$ is the quaternions vector, $\boldsymbol{\omega} = [\omega_x \quad \omega_y \quad \omega_z]^T$ is the angular velocity vector in the body frame, $\mathbf{I}$ is the matrix of inertia of the asteroid, $\mathbf{M}_c$ is the control torque, and $\boldsymbol{\Pi}$ is given by:

$$\boldsymbol{\Pi} = \begin{bmatrix} 0 & \omega_z & -\omega_y & \omega_x \\ -\omega_z & 0 & \omega_x & \omega_y \\ \omega_y & -\omega_x & 0 & \omega_z \\ -\omega_1 & -\omega_y & -\omega_z & 0 \end{bmatrix} \tag{23}$$

Perturbative torques from the Sun light pressure and the YORP effect are neglected because their cumulative effect is negligible with respect to the torque induced by the laser.

A strategy to reduce the spinning rate of the asteroid is to apply a control torque proportional to the opposite of the angular velocity vector:

$$M_c \sim -\frac{\omega}{\|\omega\|} \tag{24}$$

The actual control torque M_c that can be generated is given by the cross product of the thrust F_L^b with the position vector s. F_L^b is the thrust vector, projected in body axes, produced by the ablation process at point s on the surface of the asteroid (see Figure 5a).
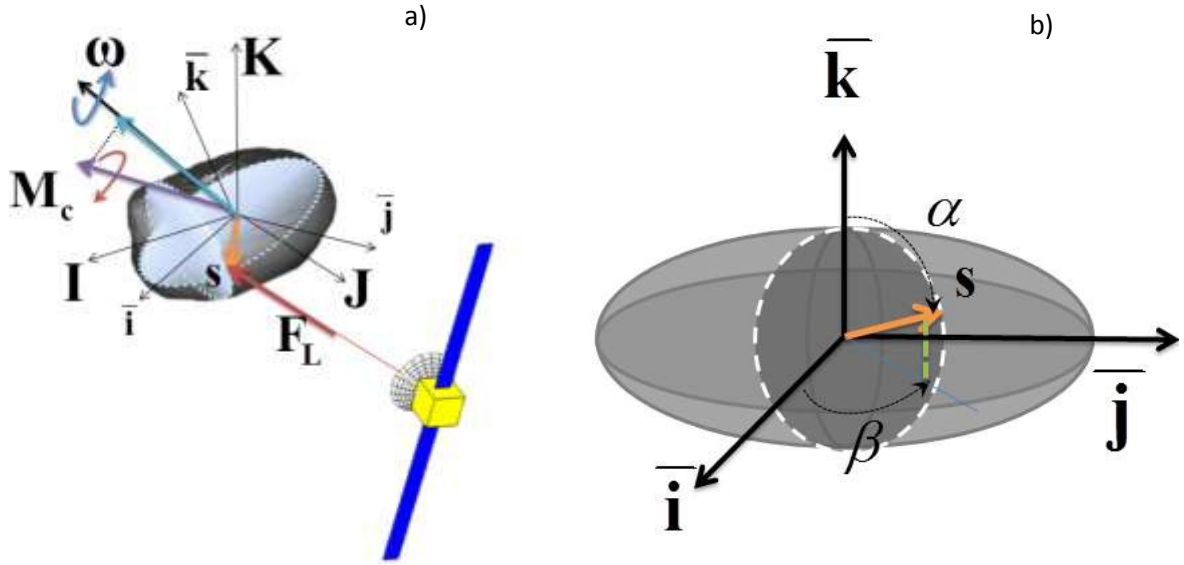
Figure 5: Angular velocity control scheme (a); control arm representation in body frame (b).

In the following it is assumed that the asteroid is an ellipsoid with a regular and smooth surface, and that the F_L^b is aligned with the vector normal to the surface and pointing inside the body of the asteroid. The normal n to the surface can be calculated as the gradient of the surface function as follows:

$$n = \nabla(s'A(t)s - 1)/\|\nabla(s'A(t)s)\| = \left[\frac{s_x^b}{a_l^2} \quad \frac{s_y^b}{b_l^2} \quad \frac{s_z^b}{c_l^2}\right] \Big/ \left\|\frac{s_x^b}{a_l^2} \quad \frac{s_y^b}{b_l^2} \quad \frac{s_z^b}{c_l^2}\right\| \tag{25}$$

The achievable control torque then becomes:

$$M_c = s \times F_L^b = F_L \left[\frac{s_y^b s_z^b}{c_l^2} - \frac{s_y^b s_z^b}{b_l^2} \quad \frac{s_x^b s_z^b}{a_l^2} - \frac{s_x^b s_z^b}{c_l^2} \quad \frac{s_x^b s_y^b}{b_l^2} - \frac{s_x^b s_y^b}{a_l^2}\right] \Big/ \left\|\frac{s_x^b}{a_l^2} \quad \frac{s_y^b}{b_l^2} \quad \frac{s_z^b}{c_l^2}\right\| \tag{26}$$

With reference to Figure 5b, it is convenient to parameterise the position of a point on the surface with the two angles α and β:

$$s_x^b = a_l \sin\alpha \cos\beta$$
$$s_y^b = b_l \sin\alpha \sin\beta \tag{27}$$
$$s_z^b = c_l \cos\alpha$$

where β is the azimuth and α is the polar angle taken from the minor semi-major axis (see Figure 5b). The achievable torque then can be rewritten as:

$$\mathbf{M}_c = \frac{1}{2} \frac{F_L}{\sqrt{\left(\frac{\sin\alpha\cos\beta}{a_I}\right)^2 + \left(\frac{\sin\alpha\sin\beta}{b_I}\right)^2 + \left(\frac{\cos\alpha}{c_I}\right)^2}} \begin{bmatrix} \sin\beta\sin2\alpha\left(\frac{b_I^2 - c_I^2}{b_I c_I}\right) \\ \cos\beta\sin2\alpha\left(\frac{c_I^2 - a_I^2}{a_I c_I}\right) \\ \sin2\beta\sin^2\alpha\left(\frac{a_I^2 - b_I^2}{a_I b_I}\right) \end{bmatrix} \qquad (28)$$

The required control toque is given by the projection of $\mathbf{M}_c$ on the angular velocity vector:

$$M_\omega = \mathbf{M}_c \cdot \boldsymbol{\omega} =$$

$$= \frac{F_L}{2} \frac{\sin\alpha\left(c_z\left(\frac{a_I^2 - b_I^2}{a_I b_I}\right)\sin\alpha\sin2\beta + 2c_y\left(\frac{c_I^2 - a_I^2}{a_I c_I}\right)\cos\alpha\cos\beta + 2c_x\left(\frac{b_I^2 - c_I^2}{b_I c_I}\right)\cos\alpha\sin\beta\right)}{\sqrt{\left(\frac{\sin\alpha\cos\beta}{a_I}\right)^2 + \left(\frac{\sin\alpha\sin\beta}{b_I}\right)^2 + \left(\frac{\cos\alpha}{c_I}\right)^2}} = F_L r_{eq} \qquad (29)$$

where c_x, c_y, c_z are the cosine directors of the angular velocity in the body frame and $r_{eq} = (\mathbf{s} \times \mathbf{n}) \cdot \boldsymbol{\omega}$ is here called *equivalent control arm*. A way to derive the point of application of the laser, given by the two angles α and β would be to solve the following maximization problem:

$$\max_{\alpha,\beta} M_\omega(\alpha,\beta) =$$

$$= \max_{\alpha,\beta} \frac{F_L(\alpha,\beta)}{2} \frac{\sin\alpha\left(c_z\left(\frac{a_I^2 - b_I^2}{a_I b_I}\right)\sin\alpha\sin2\beta + 2c_y\left(\frac{c_I^2 - a_I^2}{a_I c_I}\right)\cos\alpha\cos\beta + 2c_x\left(\frac{b_I^2 - c_I^2}{b_I c_I}\right)\cos\alpha\sin\beta\right)}{\sqrt{\left(\frac{\sin\alpha\cos\beta}{a_I}\right)^2 + \left(\frac{\sin\alpha\sin\beta}{b_I}\right)^2 + \left(\frac{\cos\beta}{c_I}\right)^2}} \qquad (30)$$

Figure 6a shows the maximum achievable projection of the control torque on the rotation velocity vector for different configurations of the ellipsoid assuming that the impinging laser beam is directed as the local normal. The rotation velocity is directed as the axis $\hat{\mathbf{z}}_h$ for each configuration. The different configurations are obtained by rotating the asteroid along the axes $\hat{\mathbf{x}}_h$ and $\hat{\mathbf{z}}_h$. Figure 6b, instead, shows the misalignment between the applied torque and the angular velocity vector, for the same configurations. The solution of problem (30) produces misalignment angles of up to 60 degrees, which would generate undesirable torque components along the directions orthogonal to the angular velocity. This effect is due to the direction of the thrust generated by the ablation process. Thus, a different strategy is to solve the following problem:

$$\max_{\alpha,\beta} r_{eq}(\alpha,\beta) =$$

$$= \max_{\alpha,\beta} \frac{1}{2} \frac{\sin\alpha\left(c_z\left(\frac{a_I^2 - b_I^2}{a_I b_I}\right)\sin\alpha\sin2\beta + 2c_y\left(\frac{c_I^2 - a_I^2}{a_I c_I}\right)\cos\alpha\cos\beta + 2c_x\left(\frac{b_I^2 - c_I^2}{b_I c_I}\right)\cos\alpha\sin\beta\right)}{\sqrt{\left(\frac{\sin\alpha\cos\beta}{a_I}\right)^2 + \left(\frac{\sin\alpha\sin\beta}{b_I}\right)^2 + \left(\frac{\cos\beta}{c_I}\right)^2}} \qquad (31)$$

Figure 6c and d show that if one optimises r_{eq}, the maximum achievable torque is lower but the maximum angle between the control torque and the angular velocity is about 35 degrees. Hence, even though

optimising r_{eq} yields a lower control torque with respect to the maximisation of M_{ω}, it has the beneficial effect of reducing the misalignment between $\mathbf{M}_c$ and $\boldsymbol{\omega}$ for each spacecraft-asteroid configuration.
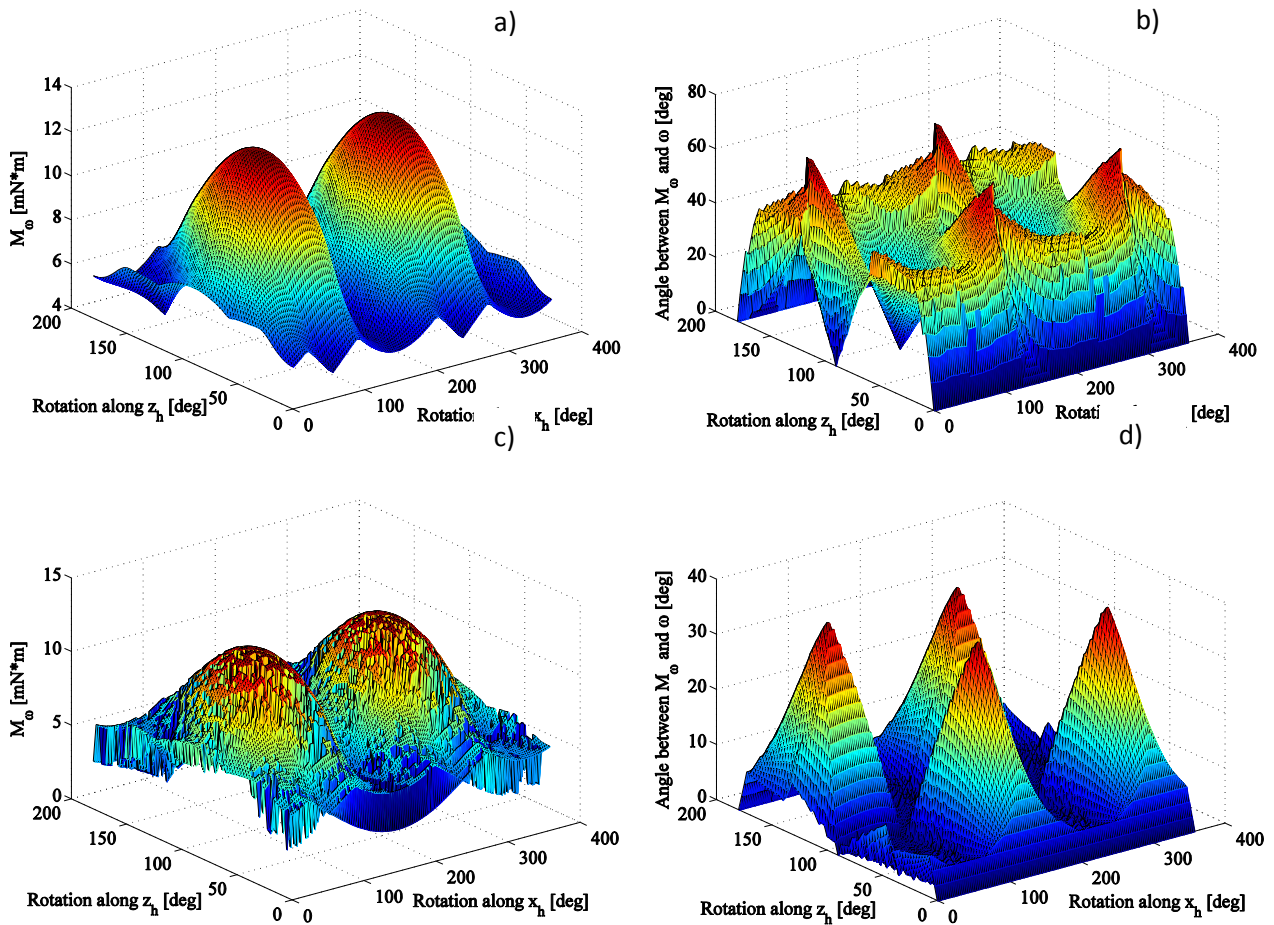
Figure 6. Maximum achievable torque: a) optimizing maximum torque M_{ω} **c) optimising** r_{eq}. **Angle between control torque and the angular velocity: b) optimising maximum torque** M_{ω} **d) optimising** r_{eq}.

Figure 7a shows the modulus of r_{eq} and the point of application of the laser for a particular configuration of the asteroid at an instant of time in which the body axes are aligned with the Hill's axes and the angular velocity is aligned with $\hat{\mathbf{z}}_h$. The colour scale in Figure 7b corresponds to the magnitude of r_{eq} for each location on the surface of the ellipsoid. Negative values refer to a torques increasing the angular velocity. This is a trivial case for which no constraint given by the configuration and the visibility from the spacecraft is imposed. The maxima are localised along the equator of the ellipsoid with azimuth angles of 132 and 312 degrees, which depend on the value of the ratio between a_l and b_l.
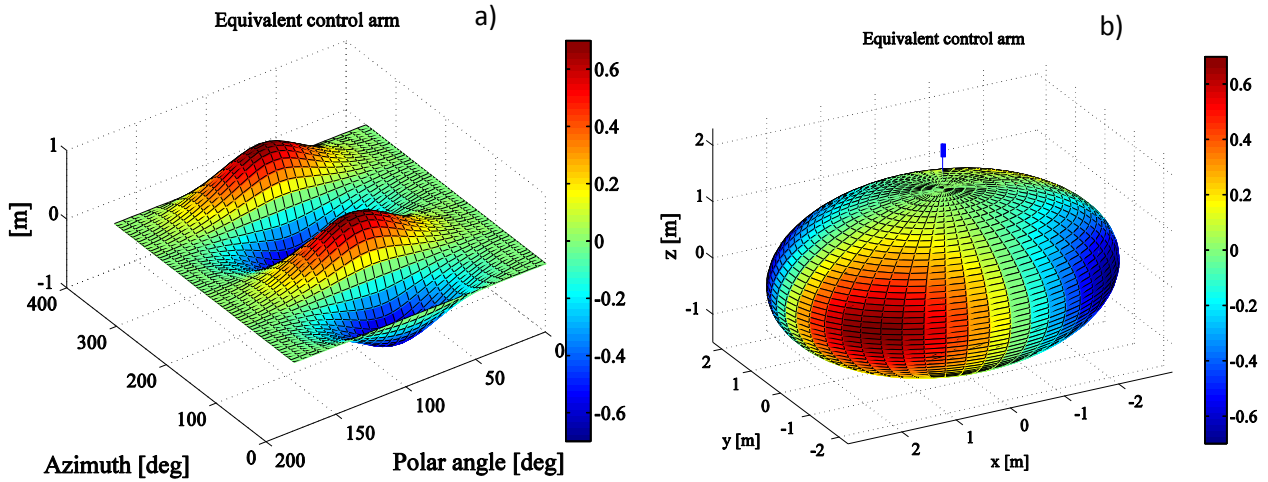
Figure 7. Equivalent control arm a) with respect to azimuth and polar angles, b) on the ellipsoid surface.

In the following, two constraints are imposed. One constraint is on the minimum angular velocity to be controlled. The asteroid angular velocity control is applied until the angular velocity reaches a value of 10^{-3} rad/s. This value has been chosen after considering that the optical flow implemented as in Section 5.2 achieves an accuracy of comparable magnitude. The second constraint is on the relative asteroid-spacecraft configuration which will limit the region the laser could be pointed at and, subsequently, also the angle between laser beam direction and local normal. In this case a limit angle of 60 degrees between the local normal and the line of sight from the spacecraft to the spot was set to avoid nearly tangent conditions for the laser. The limit on the view angle partially account for the change in spot size due to the elevation of the beam over the surface of the asteroid. Note that a non smooth surface could lead to a thrust that is not aligned with the local normal, however, since the surface that the laser can hit must be visible from the spacecraft, a torque opposite to the one expected assuming an expansion along the local normal is not possible. It is instead possible that the thrust vector and the vector connecting the spot with the barycentre from an angle that closer to 90 degrees producing a higher torque than expected. These effects due to the surface morphology will the subject of a future work.

5   Proximity and Rotational Motion Reconstruction

The motion of the spacecraft relative to the asteroid and the asteroid's rotational velocity are estimated by combining optical measurements from a camera with ranging information from a laser range finder and measurements from an impact sensor. The impact sensor, in particular, is used to measure the change in momentum due to the flow of ejecta impinging the spacecraft. The measurements then are processed through an Unscented Kalman Filter (UKF) (Schaub, 2003). Section 5.1 illustrates the measurement model. Then, Section 5.2 describes the proximity motion reconstruction while Section 5.3 shows the rotational motion reconstruction from optical flow measurements.

5.1   Measurement model

Assuming a *pinhole* model for the camera (Johnston et al., 1999), a point on the surface of the asteroid, with position $\mathbf{r_c} = [x_c \quad y_c \quad z_c]^T$ in the reference frame of the camera, has coordinates on the image plane given by:

$$\begin{bmatrix} u \\ v \end{bmatrix} = \frac{f}{x_c} \begin{bmatrix} y_c \\ z_c \end{bmatrix} \qquad (32)$$

where x_c is the distance of the point from the image plane along the boresight direction and f is the focal length of the camera. The position in the camera reference frame is given by:

$$\mathbf{r}_c = \mathbf{R}_{HC} \mathbf{x}_{Surf-SC} \qquad (33)$$

where $\mathbf{R}_{HC}$ is the rotation matrix from the Hill's reference frame to the camera frame and:

$$\mathbf{x}_{Surf-SC} = \mathbf{x}_{surface} - \delta \mathbf{r}^h \qquad (34)$$

with $\mathbf{x}_{surface}$ the vector position of the points with respect to the centre of the Hill's reference frame (see Figure 8).
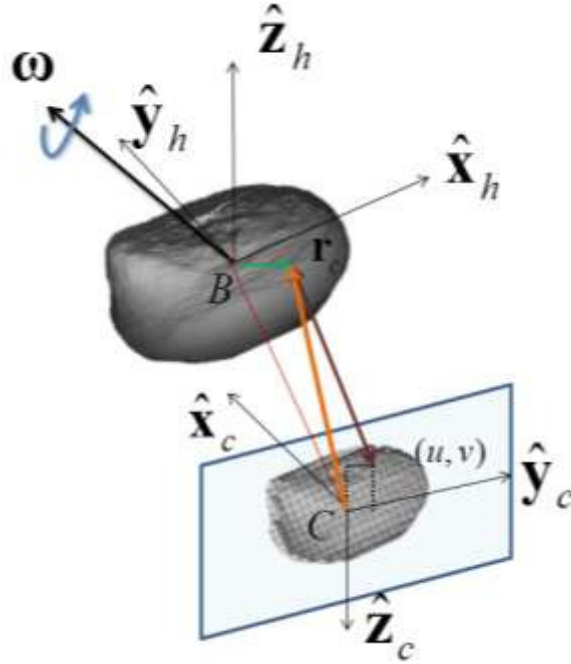
Figure 8. Pin-Hole Camera Model.

The coordinates of the point on the image plane measured in pixels are given by:

$$x_{screen} = u/p_{width}$$
$$y_{screen} = v/p_{width} \qquad (35)$$

with p_{width} the pixel width.

The mean position of all the points on the image plane of the camera defines the coordinates of the centroid of the asteroid $({}^c x_c, {}^c y_c)$. It is assumed that the centroid of the asteroid identifies the position of the centre of mass, therefore by measuring the angular position of the centroid one can estimate the angular position of the centre of mass in the reference frame of the camera. The azimuth and elevation angles of the centroid are given by:

$$\varphi = \tan^{-1} \frac{{}^c x_c}{f}$$

$$\psi = \tan^{-1} \frac{{}^c y_c}{\sqrt{{}^c x_c^2 + f^2}}$$

(36)

The measurement from the camera is affected by both the spacecraft attitude pointing and pixelization errors. The latter error is due to the fact that the image of the asteroid is formed by a discrete number of pixels and this could lead to an incorrect position of a surface feature on the image plane. By manipulating Eq. (36) and considering the pixelization error ς_p, one can write the observation equation:

$$\mathbf{z}_{camera} = \begin{bmatrix} \tan^{-1} \dfrac{{}^c u_c p_{width} + \varsigma_p}{f} \\[3mm] \tan^{-1} \dfrac{{}^c v_c p_{width} + \varsigma_p}{\sqrt{({}^c u_c p_{width} + \varsigma_p)^2 + f^2}} \end{bmatrix}$$

(37)

By expanding Eq. (37) up to the first order in the noise component, one obtains:

$$\mathbf{z}_{camera} = \begin{bmatrix} \tan^{-1} \dfrac{{}^c u_c p_{width}}{f} \\[3mm] \tan^{-1} \dfrac{{}^c v_c p_{width}}{\sqrt{({}^c u_c p_{width})^2 + f^2}} \end{bmatrix} + \ldots$$

$$+ \begin{bmatrix} \dfrac{1}{\sqrt{1 + \left(\dfrac{{}^c u_c p_{width}}{f}\right)^2}} \dfrac{\varsigma_p}{f} \\[6mm] \dfrac{1}{\sqrt{1 + \left(\dfrac{{}^c v_c p_{width}}{\sqrt{({}^c u_c p_{width})^2 + f^2}}\right)^2}} \left(\dfrac{1}{\sqrt{\left(\dfrac{{}^c u_c p_{width}}{f}\right)^2 + 1}} - \dfrac{\left({}^c u_c p_{width}\right)\left({}^c v_c p_{width}\right)}{f^2 \sqrt{\left(\left(\dfrac{{}^c u_c p_{width}}{f}\right)^2 + 1\right)^3}} \right) \dfrac{\varsigma_p}{f} \end{bmatrix} + O(\varsigma_p^2)$$

(38)

From Eq. 34 one can see that the worst case error is achieved when the point is located at the centre of the screen. This means that in the worst case

$$\mathbf{z}_{camera} \leq \begin{bmatrix} \tan^{-1} \dfrac{{}^c u_c p_{width}}{f} \\[3mm] \tan^{-1} \dfrac{{}^c v_c p_{width}}{\sqrt{({}^c u_c p_{width})^2 + f^2}} \end{bmatrix} + \begin{bmatrix} \dfrac{\varsigma_p}{f} \\[3mm] \dfrac{\varsigma_p}{f} \end{bmatrix}$$

(39)

So the model for the observation equations used in the filter becomes:

$$\mathbf{z}_{camera} = h_{camera}(\delta\mathbf{r}, \mathbf{q}) + \boldsymbol{\varsigma}_{camera} = \begin{bmatrix} \tan^{-1} \dfrac{{}^{c}u_c p_{width}}{f} \\[4mm] \tan^{-1} \dfrac{{}^{c}v_c p_{width}}{\sqrt{({}^{c}u_c p_{width})^2 + f^2}} \end{bmatrix} + \begin{bmatrix} \dfrac{\varsigma_p}{f} \\[4mm] \dfrac{\varsigma_p}{f} \end{bmatrix} \tag{40}$$

It is here assumed that the whole surface facing the spacecraft is visible, without considering illumination constraints. This does not affect the validity of the results, because, prior to the beginning of the ablation process, a precise map of the asteroid is assumed to be available. The distance from the point on the surface that corresponds to the centroid is measured through a Laser Range Finder (LRF). This distance is simply given by:

$$l = \left| \delta\mathbf{r}^h - \mathbf{x}^c_{surface} \right| \tag{41}$$

where $\mathbf{x}^c_{surface}$ is the position of the point on the asteroid's surface along the centroid direction. The observation equation of the LRF including the measurement noise reads:

$$z_l = h_l\left(\delta\mathbf{r}^h\right) + \varsigma_l = l + \varsigma_l \tag{42}$$

with ς_l a white measurement noise.

An impact sensor is used to measure the mass flow from the ablation process. These sensors provide information on the mean velocity and the mass flow per unit area of the ejecta plume. These can be used to estimate the force exerted by the ejecta plume as:

$$F_{plume} = \dot{m}_{laser}\bar{v}_s A_{S/C-attitude} = m_{SC} a_{plume} \tag{43}$$

where $\dot{m}_{laser}$ is the mean mass flow per unit area, $\bar{v}_s$ is the mean ejecta velocity at the spacecraft, $A_{S/C-attitude}$ is the cross section of the spacecraft with respect to the ejection velocity (which depends on spacecraft attitude) and it is assumed to be equal to A_{eq} as in Eq. (18). The value of the term a_{plume} in Eq.(43) is estimated as part of the filtering process in Section 5.2. The observation equation is, thus, given as

$$z_{plume} = h_{rel}\left(a_{plume}\right) + \varsigma_{plume} = m_{SC} a_{plume} + \varsigma_{plume} \tag{44}$$

where ς_{plume} is the zero-mean Gauss white measurement noise.

The full set of observation equations is given by:

$$\mathbf{z} = h(\delta\mathbf{r}^h, \mathbf{q}, a^h_{plume}) + \boldsymbol{\varsigma} = \begin{bmatrix} h_{camera}(\delta\mathbf{r}, \mathbf{q}) & h_l(\delta\mathbf{r}^h) & h_{plume}(a^h_{plume}) \end{bmatrix}^T + \begin{bmatrix} \varsigma_{camera} & \varsigma_l & \varsigma_{plume} \end{bmatrix}^T \tag{45}$$

where ς comprises the measurement noises of all the sensors.

5.2 Proximity motion reconstruction

Given the non-linearities in the measurements and dynamics, it was decided to use an Unscented Kalman Filter to derive an estimate of the state and $\mathbf{a}_p$. In order for the proposed proximity control to work, the state of the spacecraft needs to be known quite accurately (Vasile et al., 2013) while $\mathbf{a}_p$ is required only when the correction manoeuvre is performed. The need for an accurate estimation descends directly by the control box definition, being required to maintain the spacecraft within 0.4 m. As a

consequence the accuracy must be better than 0.4, otherwise the controller will be not able to allocate manoeuvres properly.

In order to maintain the desired distance from the surface of the asteroid, the control strategy requires the determination of the state vector $[\delta\mathbf{r}^h, \delta\dot{\mathbf{r}}^h]^T = [x_h, y_h, z_h, v_{x_h}, v_{y_h}, v_{z_h}]^T$ and an estimation of the acceleration $\mathbf{a}_p$ (see Eq. (21)).

The components of $\mathbf{a}_p$ due to the laser recoil and solar radiation pressure are assumed to be well known because the acceleration due to solar pressure can be precisely estimated before the deflection operations begin and the laser recoil can be tested on ground. The component of $\mathbf{a}_p$ that cannot be estimated only relying on models is the one due to the laser ablation itself, given the expected large degree of uncertainty in the outcome of the ablation process.

If the acceleration induced by the ablation a_L^h and the one due to the plume impingement a_{plume} were aligned, the camera and the LRF would suffice to determine the overall acceleration. Indeed, the acceleration induced by the plume impingement is directed along the asteroid-spacecraft direction, but the acceleration on the asteroid is directed along the local normal to the surface.

It would not be possible to estimate a_{plume} and a_L^h without any additional information. The impact sensor gives the necessary information.

The proposed method is the one used to estimate biases, commonly implemented to estimate solar radiation pressure (Maybeck, 1979). In this case, it consists in augmenting the state vector that the Unscented Kalman Filter needs to determine by two variables $[a_L^h, a_{plume}]^T$. The augmented state vector then becomes $\mathbf{x} = [\delta\mathbf{r}^h, \delta\dot{\mathbf{r}}^h, a_L^h, a_{plume}]^T = [x_h, y_h, z_h, v_{x_h}, v_{y_h}, v_{z_h}, a_L^h, a_{plume}]^T$ and the augmented dynamics reads as:

$$
\begin{aligned}
\begin{bmatrix} \dot{x}_h \\ \dot{y}_h \\ \dot{z}_h \end{bmatrix} &= \begin{bmatrix} v_{x_h} \\ v_{y_h} \\ v_{z_h} \end{bmatrix} \\[2ex]
\begin{bmatrix} \dot{v}_{x_h} \\ \dot{v}_{y_h} \\ \dot{v}_{z_h} \end{bmatrix} &= -\ddot{\mathbf{r}}_{a-g}^h - 2\dot{\boldsymbol{\theta}}^h \times \delta\dot{\mathbf{r}}^h - \dot{\boldsymbol{\theta}}^h \times \delta\mathbf{r}^h - \dot{\boldsymbol{\theta}}^h \times (\dot{\boldsymbol{\theta}}^h \times \delta\mathbf{r}^h) - \frac{\mu_{sun}}{r_{Sc}^3}(\delta\mathbf{r}^h + \mathbf{r}_a^h) + \mathbf{a}_p + \mathbf{w}_{sc} \\[2ex]
a_L^h &= 0 + w_L \\
a_{plume} &= 0 + w_{plume}
\end{aligned}
\tag{46}
$$

where $\mathbf{w}_{sc}$, w_L and w_{plume} are system noises. The process noise $\mathbf{w}_{sc}$ is a vector with three components each of which has a value of 10^{-9} km/s^2, 1-sigma, unbiased, and corresponds to the expected variations of the light pressure due to the attitude error. The noise w_L is taken as 10%, 1-sigma, unbiased, of the initial acceleration due to laser ablation predicted by the model at the beginning of each simulation and w_{plume} is taken as 10%, 1-sigma, unbiased, of the acceleration due to the flow impingement measured by the impact sensor at the beginning of each simulation. Treating these accelerations as biases is a strong assumption because it implies that their dynamics is slowly varying with time and can be seen as a random process on the short time. The results in section 6.1.1 will demonstrate the effectiveness of the proposed approach. In

order to integrate Eq.(46), one needs to update the instantaneous value of r_a^h, $\dot{\theta}^h$ in Eqs. (15) and (16) with the estimated current value of the acceleration exerted on the asteroid:

$$\mathbf{a}_L^h = a_L^h \mathbf{n} \tag{47}$$

The total perturbative acceleration acting on the spacecraft is then given by:

$$\mathbf{a}_p = -a_L^h \mathbf{n} + a_{plume} \frac{\delta \mathbf{r}^h}{\delta r} + \frac{\mathbf{F}_{Solar}(\delta \mathbf{r}^h, \mathbf{r}_a^h) + \mathbf{F}_{recoil}(\delta \mathbf{r}^h, \mathbf{r}_a^h)}{m_{SC}} - \frac{\mu_a}{\delta r^3} \delta \mathbf{r}^h + \nabla U(\delta \mathbf{r}, \mathbf{q}) \tag{48}$$

where the gravity gradient depends on the spacecraft position and attitude of the asteroid.

By using the estimation theory formalism, the integration of the nonlinear discrete-time process in Eqs. (46) and measurement equations in Section 5.1 can be expressed as:

$$\mathbf{x}_{k+1} = g(\mathbf{x}_k, \mathbf{w}_k, \mathbf{q}_k)$$
$$\mathbf{z}_k = h(\mathbf{x}_k, \mathbf{q}_k) + \varsigma_k \tag{49}$$

with $\mathbf{w}_k \sim N(0, \mathbf{Q}_k)$ the system noise in Eqs.(46), $\varsigma_k \sim N(0, \mathbf{R}_k)$ is the measurements noise in Eq. (45). The matrix $\mathbf{Q}_k$ is the process noise covariance matrix and the matrix $\mathbf{R}_k$ is the measurement noise covariance matrix. The matrices $\mathbf{Q}_k$ and $\mathbf{R}_k$ are diagonal matrices in this implementation.

The UKF relies on the unscented transformation to propagate a set of suitable sigma points, drawn from the apriori covariance matrix. The set of sigma points χ_i are given as:

$$\chi_i = \begin{cases} \tilde{\mathbf{x}}_k & i = 0 \\ \tilde{\mathbf{x}}_k + \left(\sqrt{(n + \kappa_{ukf})\mathbf{P}_x + \mathbf{Q}_x}\right)_i & i = 1, 2, \ldots, n \\ \tilde{\mathbf{x}}_k - \left(\sqrt{(n + \kappa_{ukf})\mathbf{P}_x + \mathbf{Q}_x}\right)_i & i = n+1, \ldots, 2n \end{cases} \tag{50}$$

where χ_i is a matrix consisting of (2n+1) vectors, with $\kappa_{ukf} = \alpha_{ukf}^2(n + \lambda_{ukf}) - n$, κ_{ukf} is a scaling parameter, constant α_{ukf} determines the extension of these vectors around $\tilde{\mathbf{x}}_k$ and was set to be $\alpha_{ukf} = 10^{-4}$, λ_{ukf} was equal to *3-n*. The defined sigma points are transformed or propagated through the nonlinear function, the so-called unscented transformation:

$$\chi_{i,k+1} = g(\chi_{i,k}, \tilde{\mathbf{q}}_k)$$
$$\mathbf{Z}_i = h(\chi_{i,k}, \tilde{\mathbf{q}}_k) \qquad \text{i=0, 1,..., 2n} \tag{51}$$

where $\tilde{\mathbf{q}}_k$ represents the estimated attitude of the asteroid at step *k*. In order to evaluate Eq. (51), one needs to have an estimate of the attitude of the asteroid between the time steps t_k and t_{k+1}. In this work this is given by integrating the first set of equations in Eqs. (22), by using the estimated values of quaternions $\tilde{\mathbf{q}}_k$ and asteroid angular velocity $\tilde{\boldsymbol{\omega}}_k$ as follows:

$$\tilde{\mathbf{q}}_{k+1} = \tilde{\mathbf{q}}_k + \frac{1}{2}\mathbf{\Pi}(\tilde{\boldsymbol{\omega}}_k)\tilde{\mathbf{q}}_k (t_{k+1} - t_k) \tag{52}$$

Then the mean value and covariance of $\mathbf{z}$ are approximated using the weighted mean and covariance of the transformed vectors

$$\overline{\mathbf{z}} = \sum_{i=0}^{2n} W_i^{(m)} \mathbf{Z}_i$$
$$\mathbf{P}_z = \sum_{i=0}^{2n} W_i^{(c)} (\mathbf{Z}_i - \overline{\mathbf{z}})(\mathbf{Z}_i - \overline{\mathbf{z}})^T \tag{53}$$

where $W_i^{(m)}$ and $W_i^{(c)}$ are the weighted sample mean and covariance,

$$W_0^{(m)} = \kappa_{ukf} / (n + \kappa_{ukf})$$
$$W_0^{(c)} = \kappa / (n + \kappa) + (1 - \alpha_{ukf}^2 + \beta_{ukf})$$
$$W_i^{(m)} = W_i^{(c)} = \kappa_{ukf} / \left[2(n + \kappa_{ukf}) \right], \quad i = 1, 2, \dots, 2n \tag{54}$$

A value $\beta_{ukf} = 2$ is used to incorporate prior knowledge of the distribution (Crassidis and Junkins 2004). The predicted mean of the state vector $\tilde{\mathbf{x}}_k^-$, the covariance matrix $\mathbf{P}_{x,k}^-$ and the mean observation $\tilde{\mathbf{z}}_k^-$ can be approximated using the weighted mean and covariance of the transformed vectors:

$$\boldsymbol{\chi}_{k|k-1}^i = g\left(\boldsymbol{\chi}_{k-1}^i, \tilde{\mathbf{q}}_{k-1}\right)$$
$$\tilde{\mathbf{x}}_k^- = \sum_{i=0}^{2n} W_i^{(m)} \boldsymbol{\chi}_{k|k-1}^i$$
$$\mathbf{P}_{x,k}^- = \sum_{i=0}^{2n} W_i^{(c)} \left[\boldsymbol{\chi}_{k|k-1}^i - \tilde{\mathbf{x}}_k^-\right]\left[\boldsymbol{\chi}_{k|k-1}^i - \tilde{\mathbf{x}}_k^-\right]^T + \mathbf{Q}_k \tag{55}$$
$$\mathbf{Z}_{k|k-1}^i = h\left(\boldsymbol{\chi}_{k|k-1}^i, \tilde{\mathbf{q}}_k\right)$$
$$\tilde{\mathbf{z}}_k^- = \sum_{i=0}^{2n} W_i^{(m)} \mathbf{Z}_{k|k-1}^i$$

The updated covariance $\mathbf{P}_{z,k}$ and the cross correlation matrix $\mathbf{P}_{xz,k}$ are:

$$\mathbf{P}_{z,k} = \sum_{i=0}^{2n} W_i^{(c)} \left[\mathbf{Z}_{k|k-1}^i - \tilde{\mathbf{z}}_k^-\right]\left[\mathbf{Z}_{k|k-1}^i - \tilde{\mathbf{z}}_k^-\right]^T + \mathbf{R}_k$$
$$\mathbf{P}_{xz,k} = \sum_{i=0}^{2n} W_i^{(c)} \left[\boldsymbol{\chi}_{k|k-1}^i - \tilde{\mathbf{x}}_k^-\right]\left[\mathbf{Z}_{k|k-1}^i - \tilde{\mathbf{z}}_k^-\right]^T \tag{56}$$

Finally, the filter state vector $\tilde{\mathbf{x}}_k = [\tilde{x}_h, \tilde{y}_h, \tilde{z}_h, \tilde{v}_{x_h}, \tilde{v}_{y_h}, \tilde{v}_{z_h}, \tilde{a}_L^h, \tilde{a}_{plume}]^T$ and covariance updated matrix $\mathbf{P}_{x,k}$ are represented as follows

$$\tilde{\mathbf{x}}_k = \tilde{\mathbf{x}}_k^- + \mathbf{K}_{gain}\left(\mathbf{z}_k - \tilde{\mathbf{z}}_k^-\right)$$
$$\mathbf{P}_{x,k} = \mathbf{P}_{x,k}^- - \mathbf{K}_{gain}\mathbf{P}_{z,k}\mathbf{K}_{gain}^T \tag{57}$$
$$\mathbf{K}_{gain} = \mathbf{P}_{xz,k}\mathbf{P}_{z,k}^{-1}$$

where $\mathbf{K}_{\text{gain}}$ is the Kalman gain matrix. Note that, the estimation process produces $\mathbf{r}_a^h$ and $\dot{\boldsymbol{\theta}}^h$ by integrating Eqs. (15) and (16), and using the value $\tilde{a}_L$ in Eq. (57).

Once an estimated value for the position and velocity of the spacecraft in the Hill's reference frame are available, one can calculate the displacement and velocity variation from the nominal position as:

$$\mathbf{d} = [\tilde{x}_h - x_h^t \quad \tilde{y}_h - y_h^t \quad \tilde{z}_h - x_h^t]$$
$$\delta\tilde{\mathbf{r}}^h = [\tilde{v}_{x_h} \quad \tilde{v}_{y_h} \quad \tilde{v}_{z_h}]$$

(58)

where $x_h^t = 0 \, \text{m}$, $y_h^t = -50 \, \text{m}$, $z_h^t = 0 \, \text{m}$ are the components of the nominal position, while the nominal velocity is zero on all the components. The estimated perturbative acceleration is then:

$$\mathbf{a}_p = -\tilde{a}_l^h \mathbf{n} + \tilde{a}_{plume} \frac{\delta\tilde{\mathbf{r}}^h}{\delta\tilde{r}} + \frac{\mathbf{F}_{Solar}(\delta\tilde{\mathbf{r}}^h, \tilde{\mathbf{r}}_a^h) + \mathbf{F}_{recoil}(\delta\tilde{\mathbf{r}}^h, \tilde{\mathbf{r}}_a^h)}{m_{SC}} - \frac{\mu_a}{\delta r^3}\delta\tilde{\mathbf{r}}^h + \nabla U(\delta\tilde{\mathbf{r}}^h, \tilde{\mathbf{q}})$$

(59)

5.3 Asteroid Rotational Motion Reconstruction

In order to control the rotational motion of the asteroid, it is necessary to estimate its instantaneous angular velocity. Moreover knowledge of the asteroid's angular velocity is required to compute an estimate $\tilde{\mathbf{q}}_k$ of the asteroid attitude from the prediction step of the UKF. Tracking feature points on the asteroid's surface can be used to measure the asteroid's angular velocity.

By applying the time derivative to both sides of the pin-hole camera model in Eq. (32) (Longuet-Higgins et al. 1980), one can relate the optical flow with the angular and linear velocity of the asteroid:

$$\begin{bmatrix} \dot{u} \\ \dot{v} \end{bmatrix} = \frac{f}{x_c}\begin{bmatrix} \dfrac{dy_c}{dt} \\ \dfrac{dz_c}{dt} \end{bmatrix} - \frac{f}{x_c^2}\frac{dx_c}{dt}\begin{bmatrix} y_c \\ z_c \end{bmatrix}$$

(60)

with:

$$\begin{bmatrix} \dfrac{dx_c}{dt} & \dfrac{dy_c}{dt} & \dfrac{dz_c}{dt} \end{bmatrix} = -\boldsymbol{\omega}_{B/C} \times \mathbf{p}_c^a - \mathbf{V}_{B/C}$$

(61)

The vectors $\mathbf{V}_{B/C}$ and $\boldsymbol{\omega}_{B/C}$ are respectively the linear and angular velocities of the asteroid relative to the camera, assuming that the camera is static in the Hill's reference frame. The relative velocity vector is defined as:

$$\mathbf{V}_{B/C} = \mathbf{R}_{HC}\delta\dot{\mathbf{r}}^h$$

(62)

The vector $\mathbf{p}_c^a = [x_c^a, y_c^a, z_c^a] = \mathbf{R}_{HC}\mathbf{x}_{\text{surface}}^{\text{T}}$ gives the position of a point on the surface of the asteroid with respect to the centre of the Hill's reference frame, projected onto the reference frame of the camera using Eq.(29). For a single point on the surface of the asteroid Eq. (60) can now be written as:

$$\begin{bmatrix} \dot{u} \\ \dot{v} \end{bmatrix} = \mathbf{M}(f, \mathbf{r}_c, \mathbf{p}_c^a)\begin{bmatrix} \mathbf{V}_{B/C} \\ \boldsymbol{\omega}_{B/C} \end{bmatrix}$$

(63)

with:

$$\mathbf{M}(f,\mathbf{r}_c,\mathbf{p}_c^a) = \begin{bmatrix} \dfrac{u}{x_c} & -\dfrac{f}{x_c} & 0 & -v & -\dfrac{uv}{f} & \dfrac{u^2}{f}+f\dfrac{x_c^a}{x_c} \\[4mm] \dfrac{v}{x_c} & 0 & -\dfrac{f}{x_c} & u & -\dfrac{v^2}{f}-f\dfrac{x_c^a}{x_c} & \dfrac{uv}{f} \end{bmatrix} \tag{64}$$

The angular velocity can be obtained directly from Eq. (60) or by re-arranging the equation so that the angular velocity becomes a function of the linear velocity:

$$\begin{bmatrix} \dot{u} \\ \dot{v} \end{bmatrix} = \begin{bmatrix} \dfrac{u}{x_c} & -\dfrac{f}{x_c} & 0 \\[4mm] \dfrac{v}{x_c} & 0 & -\dfrac{f}{x_c} \end{bmatrix} \mathbf{V}_{B/C} + \begin{bmatrix} -v & -\dfrac{uv}{f} & \dfrac{u^2}{f}+f\dfrac{x_c^a}{x_c} \\[4mm] u & -\dfrac{v^2}{f}-f\dfrac{x_c^a}{x_c} & \dfrac{uv}{f} \end{bmatrix} \boldsymbol{\omega}_{B/C} = \mathbf{M}_{\tilde{\boldsymbol{\omega}}_{B/C}}(f,\mathbf{r}_c)\mathbf{V}_{B/C} + \mathbf{M}_{\tilde{\mathbf{V}}_{B/C}}(f,\mathbf{r}_c)\tilde{\mathbf{V}}_{B/C} \tag{65}$$

$\mathbf{M}_{\tilde{\boldsymbol{\omega}}_{B/C}}(f,\mathbf{r}_c)$ and $\mathbf{M}_{\tilde{\mathbf{V}}_{B/C}}(f,\mathbf{r}_c)$ are the partitions of $\mathbf{M}(f,\mathbf{r}_c)$ relatively to the angular and linear velocity of the asteroid. The algorithm requires knowing the relative position and relative attitude between the spacecraft and the asteroid to determine the relative position of each feature points. The relative position and velocity of the spacecraft with respect to the centre of mass of the asteroid can be extracted from the proximity motion reconstruction. It is here assumed that the centre of mass of the asteroid and the centre of the Hill's reference frame almost coincide apart from an error $\mathbf{x}_{CoM}^{bias}$. Furthermore, it is assumed that the attitude of the asteroid at time t_0 and the position of each surface point with respect to the centre of mass are obtained from an observation campaign prior to the beginning of the ablation process. An estimation of the $\mathbf{p}_c^a$ vector at any time during the ablation process can be obtained from:

$$\tilde{\mathbf{p}}_c^a = \begin{bmatrix} \tilde{x}_c^a & \tilde{y}_c^a & \tilde{z}_c^a \end{bmatrix} = \mathbf{R}_{SC-attitude}\mathbf{R}_{HC}\tilde{\mathbf{x}}_{surface} = \mathbf{R}_{SC-attitude}\mathbf{R}_{HC}\mathbf{R}(\tilde{\mathbf{q}},\tilde{\mathbf{q}}_0)(\mathbf{x}_{surface}^0 + \mathbf{x}_{CoM}^{bias} + \boldsymbol{\varsigma}_{surface}) \tag{66}$$

where $\mathbf{x}_{surface}^0$ is the actual position of a feature point at t_0, $\boldsymbol{\varsigma}_{surface}$ is an error which derives from the camera and LRF measurements required to build a three dimensional map of the asteroid, $\mathbf{R}_{SC-attitude}$ is the attitude matrix of the spacecraft, which affects the pointing of the camera on two axes and $\mathbf{R}(\tilde{\mathbf{q}}_k,\tilde{\mathbf{q}}_0)$ is the rotation matrix from the initial asteroid's attitude $\tilde{\mathbf{q}}_0$ to the current attitude $\tilde{\mathbf{q}}$. The position of a feature point with respect to the camera then becomes:

$$\begin{aligned} \tilde{\mathbf{r}}_c = \begin{bmatrix} \tilde{x}_c & \tilde{y}_c & \tilde{z}_c \end{bmatrix} &= \mathbf{R}_{SC-attitude}\mathbf{R}_{HC}\mathbf{x}_{Surf-SC} = \mathbf{R}_{SC-attitude}\mathbf{R}_{HC}(\tilde{\mathbf{x}}_{surface} - \delta\tilde{\mathbf{r}}^h) = \\ &= \mathbf{R}_{SC-attitude}\mathbf{R}_{HC}\left(\mathbf{R}(\tilde{\mathbf{q}}_k,\tilde{\mathbf{q}}_0)(\mathbf{x}_{surface}^0 + \mathbf{x}_{CoM}^{bias} + \boldsymbol{\varsigma}_{surface}) - \delta\tilde{\mathbf{r}}^h\right) \end{aligned} \tag{67}$$

If one then introduces the pixelisation error then the two matrices in Eq.(65) become:

$$
\mathbf{M}_{\tilde{\boldsymbol{\omega}}_{B/C}}(f,\mathbf{r}_c)=
\begin{bmatrix}
-\dfrac{(vp_{width}+\varsigma_p)}{p_{width}} & -\dfrac{(up_{width}+\varsigma_p)(vp_{width}+\varsigma_p)}{p_{width}^2 f} & \dfrac{(up_{width}+\varsigma_p)^2}{f}+f\dfrac{\tilde{x}_c^a}{\tilde{x}_c} \\[3mm]
\dfrac{(up_{width}+\varsigma_p)}{p_{width}} & -\dfrac{(vp_{width}+\varsigma_p)^2}{p_{width}^2 f}-f\dfrac{\tilde{x}_c^a}{\tilde{x}_c} & \dfrac{(up_{width}+\varsigma_p)(vp_{width}+\varsigma_p)}{p_{width}^2 f}
\end{bmatrix}
$$

$$
\mathbf{M}_{\tilde{\mathbf{v}}_{B/C}}(f,\mathbf{r}_c)=
\begin{bmatrix}
\dfrac{(up_{width}+\varsigma_p)}{p_{width}\tilde{x}_c} & -\dfrac{f}{\tilde{x}_c} & 0 \\[3mm]
\dfrac{(vp_{width}+\varsigma_p)}{p_{width}\tilde{x}_c} & 0 & -\dfrac{f}{\tilde{x}_c}
\end{bmatrix}
$$

(68)

and $\dot{u}$ and $\dot{v}$ are approximated with $\Delta\mathbf{u}/\Delta t$ at two consecutive instants of time *k-1* and *k*. The flow field then becomes:

$$
\begin{bmatrix} \dot{u} \\ \dot{v} \end{bmatrix} = \begin{bmatrix} (u^k p_{width}+\varsigma_p^k)-(u^{k-1}p_{width}+\varsigma_p^{k-1}) \\ (v^k p_{width}+\varsigma_p^k)-(v^{k-1}p_{width}+\varsigma_p^{k-1}) \end{bmatrix} \Big/ \left(p_{width}\Delta t\right)
$$

(69)

Introducing Eqs. (66), (67), (68) and (69) into Eq. (65) and solving for the angular velocity give:

$$
\tilde{\boldsymbol{\omega}}_{B/C}=
\begin{bmatrix}
-v & -\dfrac{uv}{f} & \dfrac{u^2}{f}+f\dfrac{\tilde{x}_c^a}{\tilde{x}_c} \\[3mm]
u & -\dfrac{v^2}{f}-f\dfrac{\tilde{x}_c^a}{\tilde{x}_c} & \dfrac{uv}{f}
\end{bmatrix}^{\diamond}
\left(
\begin{bmatrix} \dot{u} \\ \dot{v} \end{bmatrix}-
\begin{bmatrix}
\dfrac{u}{\tilde{x}_c} & -\dfrac{f}{\tilde{x}_c} & 0 \\[3mm]
\dfrac{v}{\tilde{x}_c} & 0 & -\dfrac{f}{\tilde{x}_c}
\end{bmatrix}\tilde{\mathbf{V}}_{B/C}
\right)=
$$

$$
=\mathbf{M}_{\tilde{\boldsymbol{\omega}}_{B/C}}^{\diamond}(f,\mathbf{r}_c)\left(\begin{bmatrix} \dot{u} \\ \dot{v} \end{bmatrix}-\mathbf{M}_{\tilde{\mathbf{v}}_{B/C}}(f,\mathbf{r}_c)\,\tilde{\mathbf{V}}_{B/C}\right)
$$

(70)

Finally, the estimated angular velocity $\tilde{\boldsymbol{\omega}}_k$ to be used in Eq. (24) is obtained by rotating $\tilde{\boldsymbol{\omega}}_k=\mathbf{R}(\tilde{\mathbf{q}}_k)\tilde{\boldsymbol{\omega}}_{B/C}$ from the camera frame to the asteroid frame. Including other points' measurements, to give additional information and filter the error, $\boldsymbol{\omega}_{B/C}$ can be estimated using the batch least square:

$$
\boldsymbol{\omega}_{B/C}=
\begin{bmatrix}
\mathbf{M}_{\boldsymbol{\omega}_{B/C}}(f,\mathbf{r}_{c,1},\mathbf{p}_{c,1}^a) \\
\vdots \\
\mathbf{M}_{\boldsymbol{\omega}_{B/C}}(f,\mathbf{r}_{c,N},\mathbf{p}_{c,N}^a)
\end{bmatrix}^{\diamond}
\begin{bmatrix} \dot{u}_1 \\ \dot{v}_1 \\ \vdots \\ \dot{u}_N \\ \dot{v}_N \end{bmatrix}
-
\begin{bmatrix}
\mathbf{M}_{\mathbf{v}_{B/C}}(f,\mathbf{r}_{c,1},\mathbf{p}_{c,1}^a) \\
\vdots \\
\mathbf{M}_{\mathbf{v}_{B/C}}(f,\mathbf{r}_{c,N},\mathbf{p}_{c,N}^a)
\end{bmatrix}^{+}
\mathbf{V}_{B/C}
$$

(71)

where the $\diamond$ sign stands for pseudo-inverse, and all the points give equal contribution to the solution (i.e. the weight associated to their corresponding information is equal to 1). The algorithm allows extracting velocity and attitude rates from at least three tracked feature points from two consecutive frames.

As an example, Figure 9 reports the error on the estimation of the angular velocity during a 14 days operations time. A total of 10 features were considered at each time. The pixelization error ς_p is equal to the dimension of the pixel (78.5 μm according to Table 4). The asteroid surface is known with an accuracy $\varsigma_{surface}$ of 15 cm (3-σ) and the bias $\mathbf{x}_{CoM}^{bias}$ on the position of the barycentre is 20 cm (3-σ), which is equal to about 10% of the mean radius. The position and velocity of the spacecraft, $\delta\tilde{\mathbf{r}}^h$ and $\delta\dot{\tilde{\mathbf{r}}}^h$, are estimated with an accuracy of 20 cm and 0.1 mm/s (3-σ) respectively. An attitude determination error on 2 axes of 10⁻

[3] rad is also considered. The figure shows that with the assumed measurement errors, the system is able to determine the angular rate as precise as few milliradians per second.
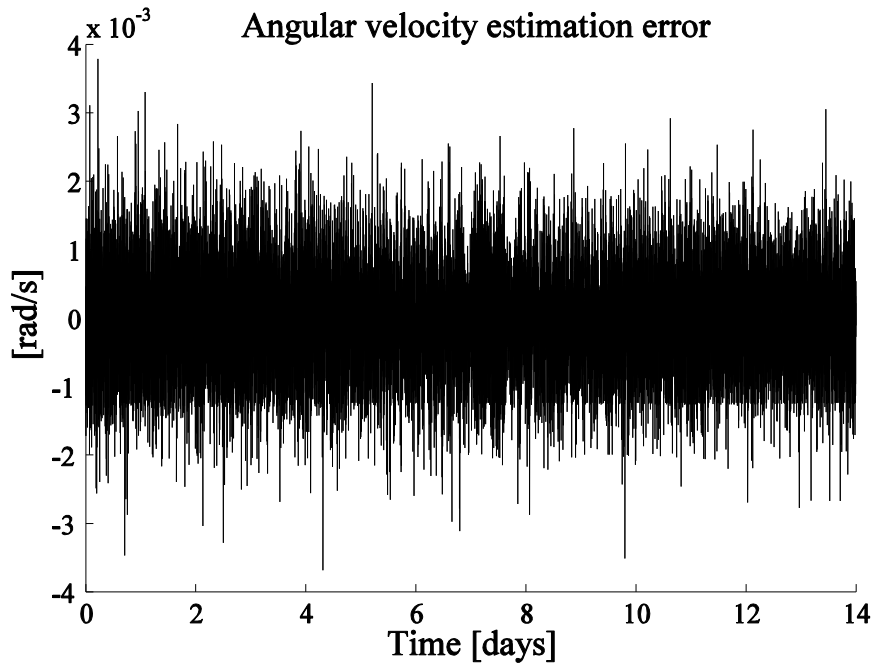

Figure 9: Angular velocity estimation error.

For sake of comparison, if one derived the angular velocity from Eq. (63) instead of Eq. (70) the accuracy would be lower, as shown in Figure 10. In the case of Eq. (63), the error is higher with respect to the case of Eq. (70) because the optical flow method is not able to extract the linear velocity as accurately as the one obtained from the Kalman filter.
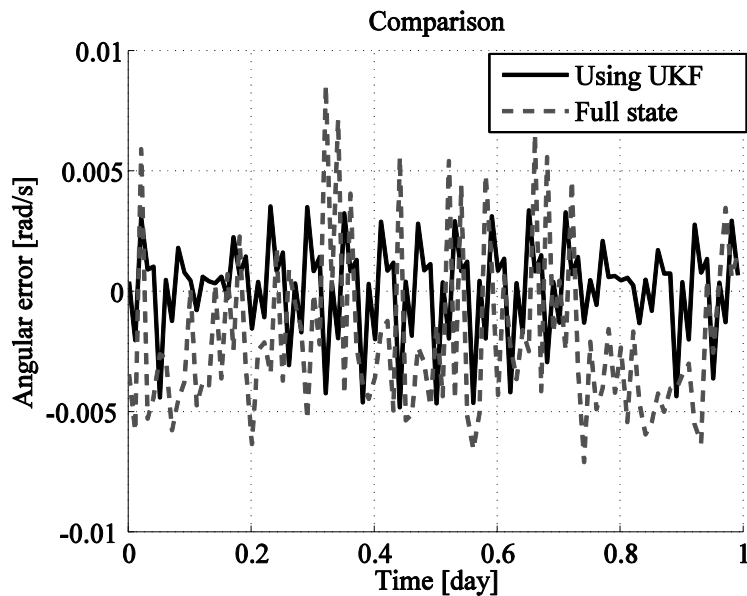
Figure 10. Angular error estimation using full state optical flow and optical flow with Kalman filter.

6 Results

The selected candidate for the deflection mission is here assumed to be the Near Earth Object 2006 RH120 whose characteristics are listed in Table 2. The criteria for the candidate selection are explained in Vasile et al., 2013.

Table 2. Orbital elements of 2006 RH120 at Epoch MJD2000 2456200.5 (12 September 2012) (http://ssd.jpl.nasa.gov/sbdb.cgi?sstr=2006%20RH120).

Orbital Element	Value
a	1.033252056035198 AU
E	0.02447403062284801
q	1.007964213574672 AU
i	0.5952660003048117 deg
node	51.14334927580387 deg
M_a	221.2498016727181 deg
t_p	2456348.356001016605 MJD2000
period	383.6258326667335 days
n	0.9384143854377558 deg/d
Q	1.058539898495724 AU

Asteroid 2006 RH120 is a small rocky asteroid with an estimated mass of 130 tonnes. It is assumed here that, the ablation process starts when the asteroid is at perihelion. The initial angular velocity is $\omega=[0.0052,0.0052,0.0332]^T$ rad/s. As before, the asteroid is assumed to be an ellipsoid with $a_l=3\,\mathrm{m}$, $b_l=2.3\,\mathrm{m}$ and $c_l=1.5\,\mathrm{m}$, and its principal axes of inertia are aligned with the Hill's frame axes at the beginning of operations. On top of the the example presented in this section the algorithm was run for different initial angular velocities and configurations. In particular it was tested on three worst case scenarios in which the largest component of ω was directed along one of the principal axis of inertia, and the matrix of inertia was dense with extra-diagonal terms with a magnitude up to 30% of the minimum inertia value. Table 3 reports the spacecraft's characteristics considered for the simulations. The spacecraft is assumed to be a cube with two symmetric deployable solar panels. The solar arrays are assumed to point towards the Sun for the whole simulation. In this way the cross section A_{eq} results to be less than 1/5 of the area A_M subjected to the solar radiation pressure.

Table 3. Spacecraft characteristics.

Element	Value
Mass	500 kg
C_R	0.18
A_M	8.4 m^2
A_{eq}	1.6 m^2

The initial state vector of the spacecraft is $\mathbf{x}_0=[0.1m \quad -50.1m \quad 0.1m \quad 10^{-4}m/s \quad 10^{-4}m/s \quad 10^{-4}m/s]^T$.

The camera is assumed to have a 30 degrees field of view, 2048 pixels resolution, and a 30 cm focal length. The focal length and resolution are such that at 50 m distance an object of approximately 4 m diameter

occupies about 10 degrees of the field of view. In this way, it is assured that the asteroid remains completely within the camera's field of view during ablation. Table 4 reports the magnitude of the errors considered during the simulation and estimation process.

Table 4. Errors in the measurements model.

Error	Value
ς_p	78.5 μm
ς_l	10 cm (1σ)
ς_{camera}	$2.6 \cdot 10^{-3}$ rad (1σ)
ς_{plume}	5% measured value (1σ)
S/C Attitude determination	10^{-3} rad on two axes (1σ)
$\mathbf{x}_{CoM}^{bias}$	20 cm (3σ)
$\varsigma_{surface}$	15 cm (3σ)

The accuracy of the LRF, ς_l, is consistent with the current state of the art for this kind of technology (Hashimoto et al. 2003). A 5% random variation in the measured mass flow rate was added to take into account a possible fluctuation in the yield of the ablation process. The attitude determination error on 2 axes is inferior to the accuracy foreseen on Hayabusa-2 (Noda et al., 2013). Moreover it was assumed that all the measurements are received and processed at the same time every 300 seconds.

6.1   Spacecraft Proximity Control

Figure 11 shows the error in the filter estimates for both position and velocity. It is assumed that the spacecraft starts ablating with an initial state estimation $\tilde{\mathbf{x}}_0 = [0.2m \quad -50.2m \quad 0.2m \quad 2 \cdot 10^{-4} m/s \quad 2 \cdot 10^{-4} m/s \quad 2 \cdot 10^{-4} m/s]^T$. From Figure 11a, the estimate is as precise as 10 cm in position, while in Figure 1a the velocity error is less than 0.1 mm/s. The higher error is along the y-component, which is almost coincident with the pointing direction of the LRF.
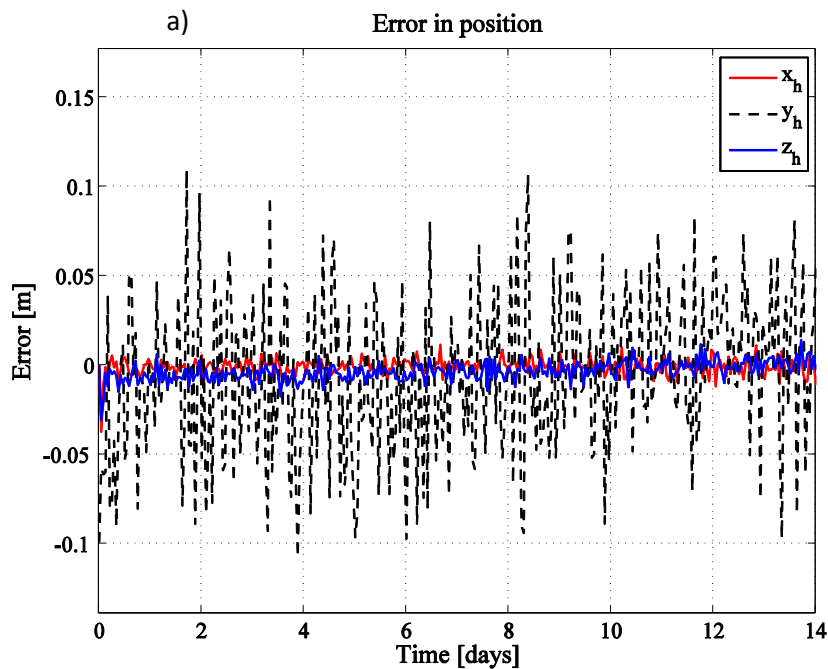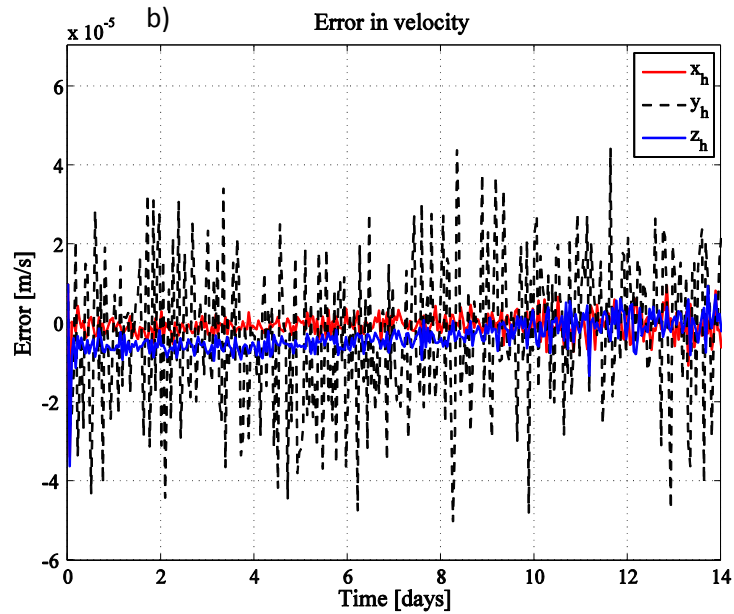
Figure 11. Spacecraft Control -Estimated position (a) and velocity error (b).

The velocity errors on $\hat{\mathbf{z}}_h$ and $\hat{\mathbf{x}}_h$ seem to converge slower although their absolute values are also lower than $\hat{\mathbf{y}}_h$. This trend is essentially caused by the estimation process of the acceleration induced by laser ablation, the magnitude of which increases as the angular velocity tends to zero. In fact the convergence towards zero is achieved when also the acceleration approaches a constant value, at about 12 days after the beginning of the ablation process (see Section 6.1.1). When one considers the actual error with respect to the desired position (i.e. spacecraft placed with zero velocity at 50 m along track), the discrete control is able to maintain the spacecraft within 0.4 m as shown in Figure 12a. For clarity we report also the norm of the controlled position error. The maximum error in velocity in Figure 12b is around 1 mm/s which is obtained at the boundaries of the control box.
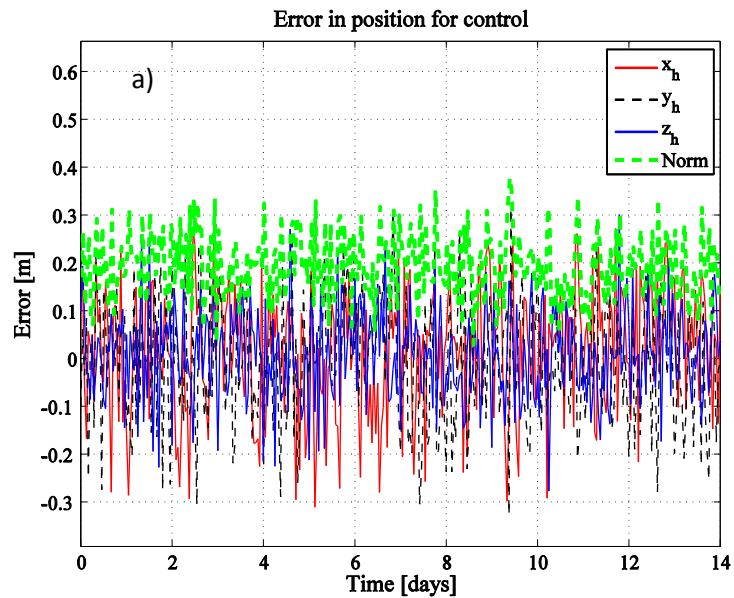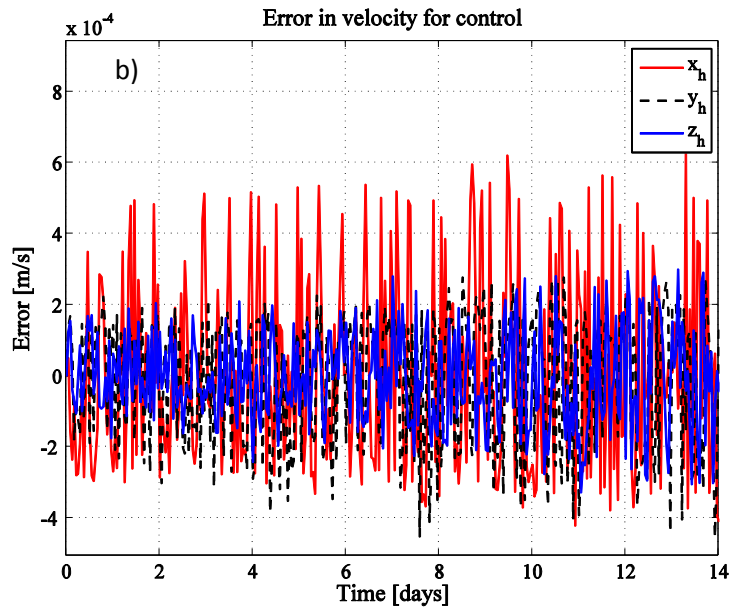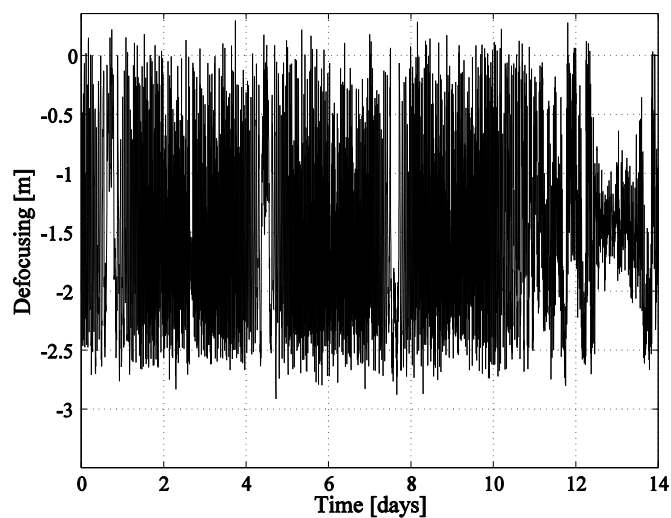
Figure 12. Discrete Control - Actual controlled position (a) and velocity error (b).

The change in sign of the velocity components is due to the actuation. Figure 12b shows that the the main perturbations are confined in the x-y plane of the Hill's frame. This is consistent with the fact that the solar radiation pressure is directed along x-axis and that the force has to be contained in the x-y plane in order to apply a control torque mainly directed as z-axis.

Nonetheless, the peaks outside the control boundaries are not detrimental to the overall process itself because their frequency and the magnitude are low, also considering the actual point the laser impinges. In fact Figure 13 reports the actual defocusing due to spacecraft and asteroid rotation control, which results contained within the Rayleigh length of 3 m.


Figure 13. Discrete Control – Actual defocusing due to spacecraft and asteroid rotation control.

Note that the combination of the visibility, rotation of the asteroid and constraint on the angle between the laser and the normal vector directions lead to impinge mainly on surface spots closer to the spacecraft (i.e. below the focussing length).

6.1.1 Estimated Perturbations During Proximity Operations

Estimating the perturbations acting on the spacecraft in real time is required to implement the control strategy defined in Section 3. Figure 14 shows the trend of the estimated perturbations due to laser ablation with respect to the actual values.
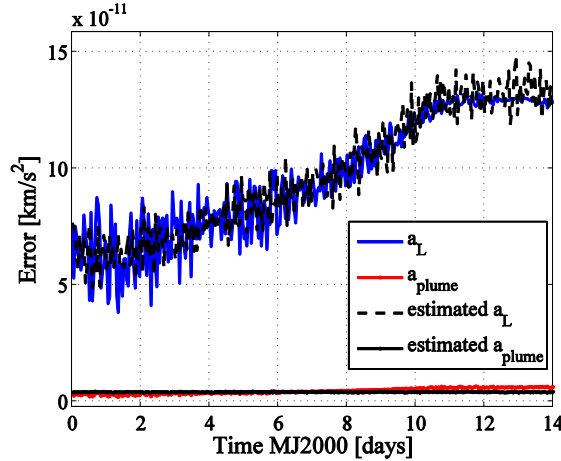

Figure 14: Estimated acceleration from the laser and plume force vs. the actual acceleration. The dashed black line is the simulated acceleration induced by the ablation process, while the continuous black line is the simulated measurement from the impact sensor.

As one can see the perturbative force due to the ablative process increases with time. This is due to the fact that the angular velocity diminishes and the efficiency of the ablative process increases. After about 12 days it converges to a nearly constant value, which corresponds to a rotational velocity of about 10^{-3} rad/s. When the asteroid reaches this rotational velocity the rotational control is terminated. The figure shows that there is a good agreement between the actual and the estimated perturbative accelerations, although the level of measurements noise affects the steady state estimate.

6.2 Asteroid Rotational Velocity Control

In the absence of any perturbation acting on the spacecraft and assuming the laser impinges perpendicular the asteroid surface, the implemented rotation control strategy would produce an effective reduction of the asteroid angular velocity in about 6.2 days as shown in Figure 15, where the components of the angular velocity in the body fixed frame are represented.
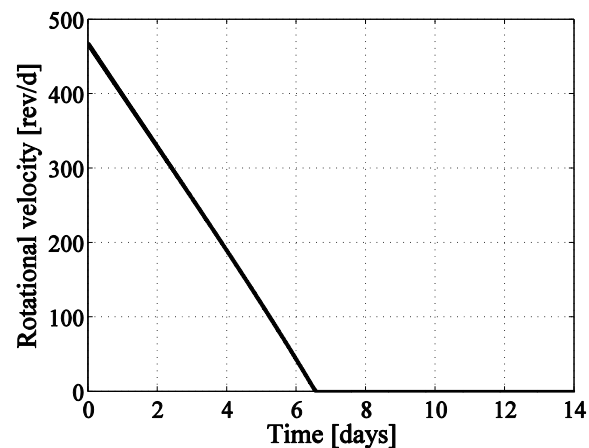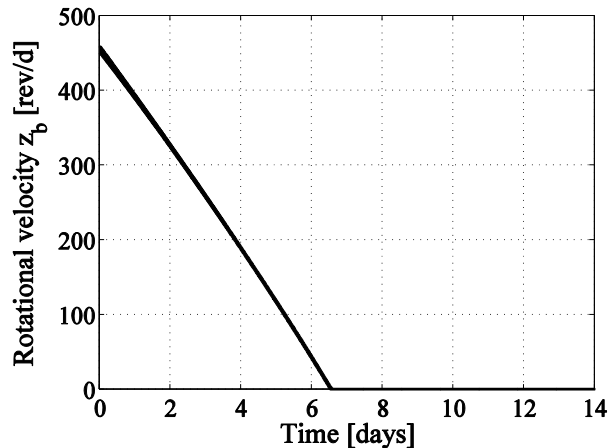
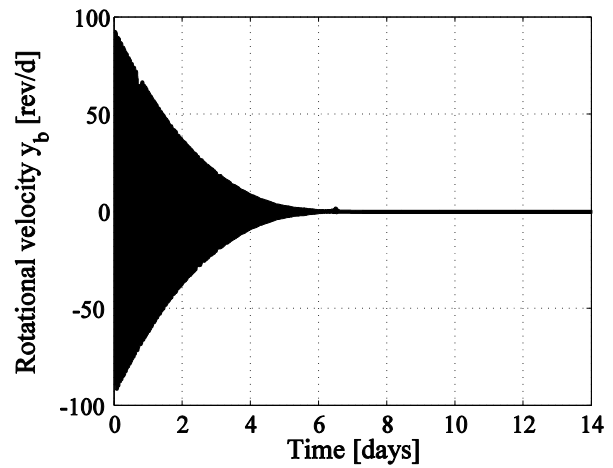
a)   b)
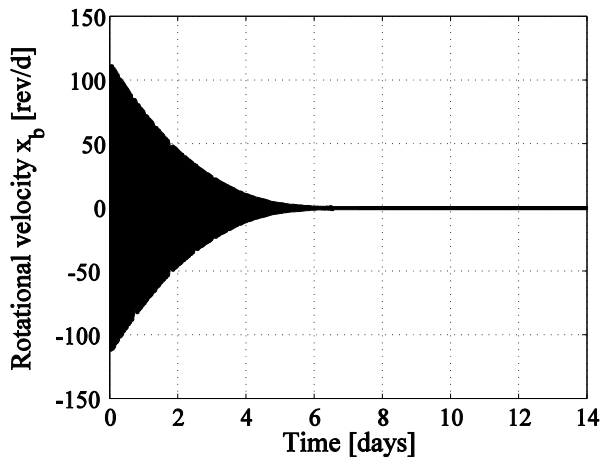
c)   d)

Figure 15. Asteroid rotation control assuming the laser impinges perpendicularly the asteroid surface. a) Absolute magnitude and z (b), x (c) and y (d) axes of the body fixed frame.

As one can see the control torque acts efficiently on the three directions. The angular velocity, as well as the third component, decreases almost monotonically as shown in Figure 15a-b. The other two components converge towards the zero velocity condition with progressively decreasing oscillations (Figure 15c-d). When the spacecraft proximity control and all the perturbation effects, as well as the angle between the laser beam and the normal to surface, are included in the model, a similar trend in a different time is obtained as shown in Figure 16. Also in this case the components of the angular velocity refers to the body fixed frame. The inertia matrix of the asteroid is almost diagonal with the extra-diagonal terms equal to 1/100 of the maximum inertia.
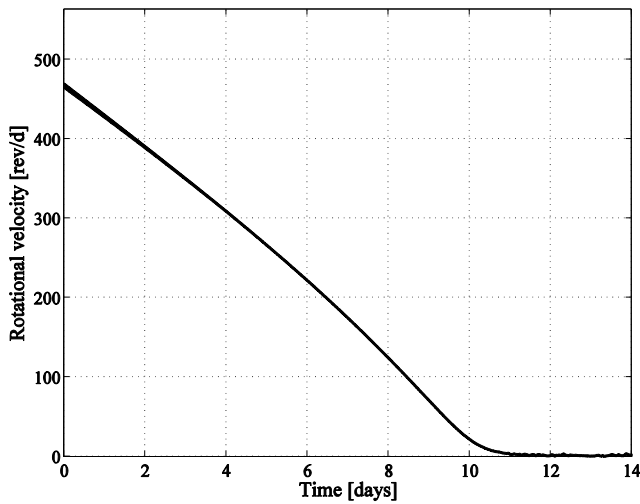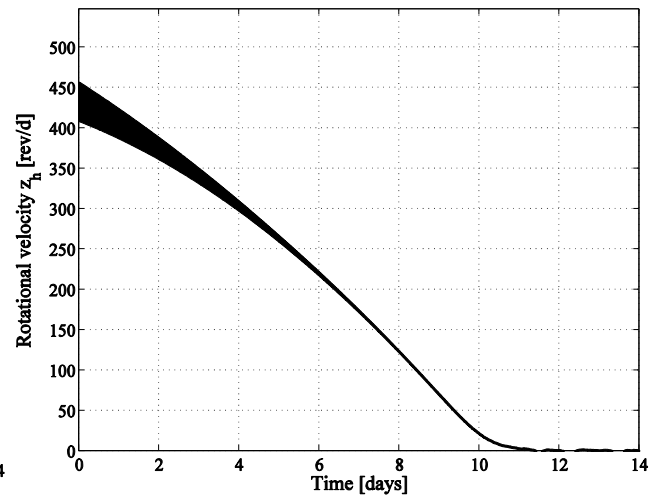
a)   b)
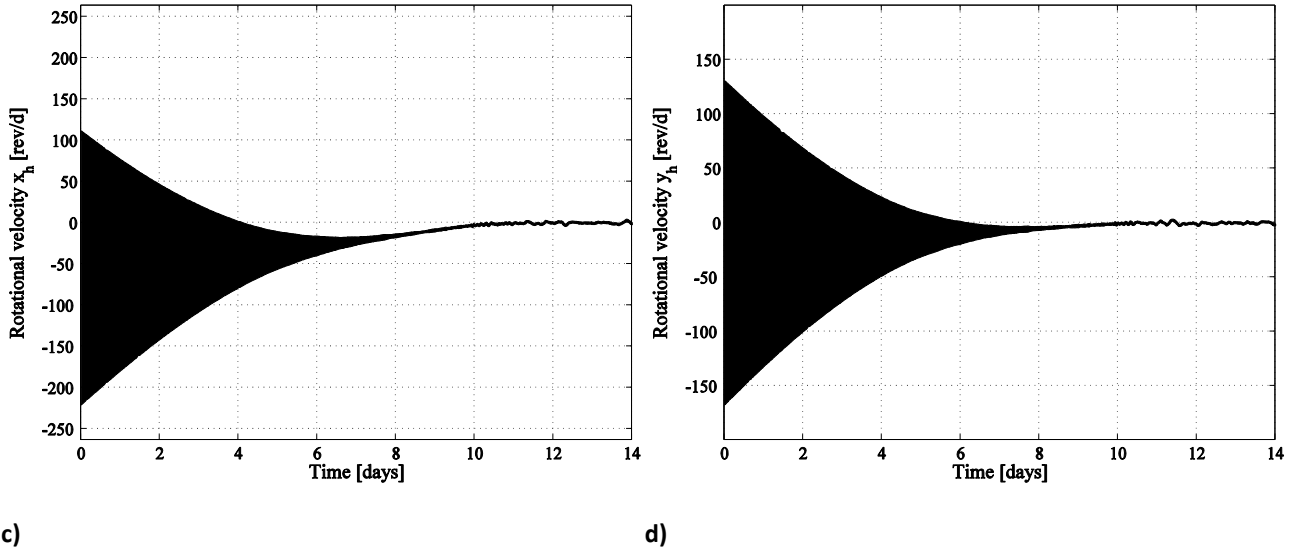
Figure 16. Rotational velocity of the asteroid considering the actual incidence of the laser. a) Absolute magnitude and z (b), x (c) and y (d) axes of the body fixed frame.

Also in this case, Figure 16a-c show a similar trend for the angular velocity and the z_b component with oscillations in the final part of the simulations. The time required to almost halt the asteroid rotation is about 12 days. It takes about 5 days more than the case where the spacecraft is fictitiously maintained fixed at 50 m from the asteroid and the laser beam cross section varies only because of the. From Figure 16c-d one can see that the other two components converge towards zero as the previous case up to 12 days, then all the components present oscillations. These are due to the fact that the main component of the angular velocity moves continuously among the components. The oscillations in the position of the spacecraft, as shown in Section 6.1, cause also the laser beam to periodically defocus. Moreover, the whole control procedure is affected by the accuracy level provided by the optical flow method and the estimated position of the spacecraft with errors in the exerted control torque.

Regarding the other tests mentioned in Section 6, we found that the worst case was the one with all the angular velocity directed along the maximum axis of inertia. It required about 18 days to converge to 10^{-3} rad/s.

7   Effect of the Asteroid's Rotation on its Deflection

The ablation thrust in Eq. (1) induces a slow and constant variation of the orbit of the asteroid. As explained in Section 4, the asteroid angular velocity control is performed until the angular velocity reaches a value of 10^{-3} rad/s. It is assumed that the deflection action on the asteroid starts at asteroid's perihelion and the rotation control is active for up to 12 days, as shown in Figure 16. It is assumed that, once the desired rotational velocity is reached, the laser beam is pointed in such a way that the rotational velocity does not vary over time. From Figure 17a it can be seen that the thrusting time to achieve a target δv_l of 1 m/s can be decreased from 400 days up to 100 days with only 12 days of control of the rotation of the asteroid.
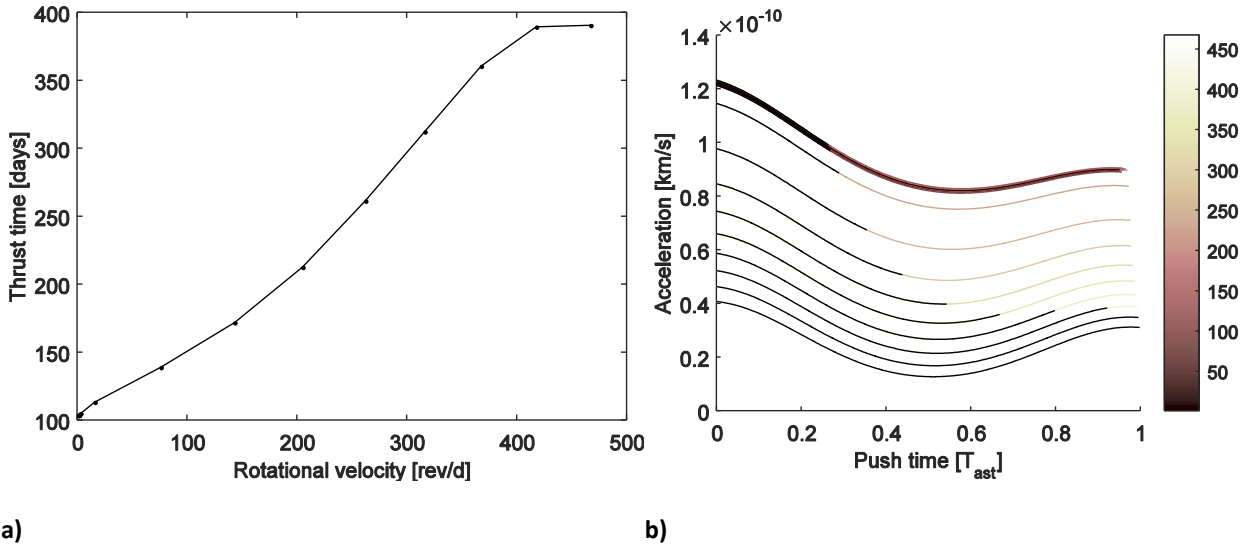
Figure 17. a) Thrust time to achieve the target delta-velocity change as function of the initial rotational velocity of the asteroid. b) Actual acceleration onto the asteroid as function of time with different initial rotational velocities of the asteroid (colour bar). The black portion of the lines represents the time needed to achieve the target change in velocity of 1 m/s.

While the target delta-velocity is independent of the direction of thrust, the effect on the displacement from its nominal position at a given point along the orbit (called check-point in the following) depends on the direction of the thrust. Let a, e, i, Ω, ω_a and M_a be respectively the semi-major axis, eccentricity, inclination, anomaly of the ascending node, anomaly of the pericentre and mean anomaly of the nominal orbit of the asteroid. The effect of the deflection is calculated at predefined check-points. Let t_{check} be the instant of time corresponding to a generic check point. If θ_{check} is the true anomaly of the asteroid, and $\theta^*_{check} = \theta_{check} + \omega_a$ the corresponding argument of latitude, one can write the variation of the position of the asteroid after deviation, with respect to its unperturbed position, by using the proximal motion equations as in (Vasile and Colombo, 2008) and (Colombo et al., 2009):

$$\delta\mathbf{r}_a\left(t_{check}\right) = \mathbf{A}_{check}\delta\boldsymbol{\alpha}\left(t_{check}\right) \tag{72}$$

where $\delta\mathbf{r}_a = \begin{bmatrix} \delta x_{h-a} & \delta y_{h-a} & \delta z_{h-a} \end{bmatrix}^T$ with δx_{h-a}, δy_{h-a} and δz_{h-a} the displacements in the radial, transversal and out of-plane directions in the Hill's reference frame centred at the unperturbed position of the asteroid at the check point (see Figure 18). The vector $\delta\boldsymbol{\alpha}(t_{check}) = \begin{bmatrix} \delta a & \delta e & \delta i & \delta\Omega & \delta\omega_a & \delta M_a \end{bmatrix}^T$ is the variation of the orbital parameters at the check-point and the matrix $\mathbf{A}_{check}$ transforms the variation of the orbital parameters in trajectory displacements.
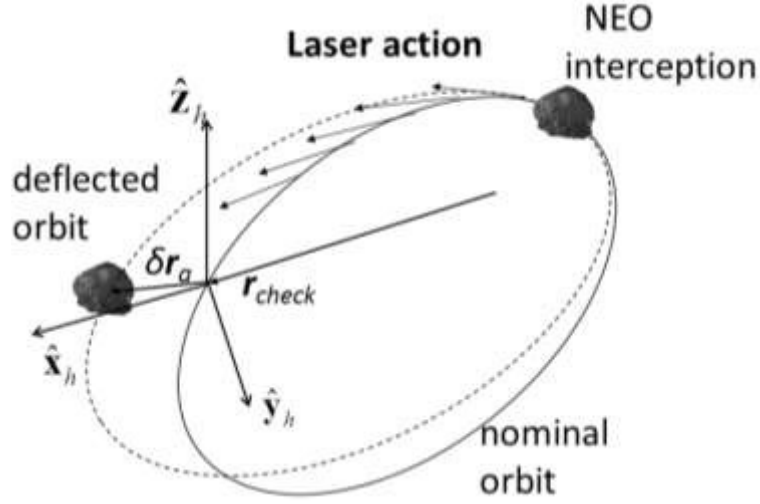
Figure 18. Asteroid's proximal motion.

The assumption used to compute Eq. (72) is that the variation of the relative position $\delta r_a = \|\delta \mathbf{r}_a\|$ is small compared to the unperturbed orbit radius r_{check}, that is $\delta r_a \ll r_{check}$.

When a low-thrust deviation action such as the one in Eq. (1) is applied over the interval $[t_i \quad t_e]$, where $t_e \le t_{check}$ is the time when the manoeuvre ends, the total variation of the orbital parameters $\delta \boldsymbol{\alpha}(t_{check})$ can be computed by integrating Gauss' planetary equations over the thrusting arc. Note that the derivative of M_a in Gauss' planetary equations

$$\frac{dM_a}{dt} = n - \frac{b}{eav}\left[2\left(1+\frac{e^2 r_a}{p}\right)\sin\theta a_t + \frac{r_a}{a}\cos\theta a_n\right]$$

takes into account the instantaneous change of the orbit geometry at each instant of time $t \in [t_i \quad t_e]$ and the variation of the mean motion n due to the change in the semi-major axis along the thrust arc. The total variation δM_a in the mean anomaly between the proximal and the unperturbed orbit was found to be (Colombo et al., 2009):

$$\delta M_a = \tilde{M}_{check} - M_{check} = (n_e - n_i)t_{check} + n_i t_i - n_e t_e + \Delta M_a \tag{73}$$

where n_i is the nominal angular velocity,

$$n_e = \sqrt{\frac{\mu_{Sun}}{(a+\Delta a)^3}}$$

is the variated angular velocity and $\Delta M = -\int_{t_i}^{t_e}\frac{b}{eav}\left[2\left(1+\frac{e^2 r_a}{p}\right)\sin\theta a_t + \frac{r_a}{a}\cos\theta a_n\right]dt$.

From Eqs. (72) one can compute the effect of the deflection action at the check-points $t_{check} = t_e$. The deflection depends on the direction of the thrust (see Vasile and Colombo, 2008) as visible in Figure 19. The figure represents the deviation in Eq. (72) achieved in the thrusting time $[t_i \quad t_e]$ as a function of the initial rotational velocity of the asteroid at time t_i. The figure reports also the ideal cases in which the thrust is

applied along the tangent (black continuous line), normal (dash line) and out-of-plane (dash bold line) direction. The bold black line corresponds to the deviation achieved with the actual thrust vector. As expected, the deflection is contained between the two extremes of pure tangential and pure normal deflections.
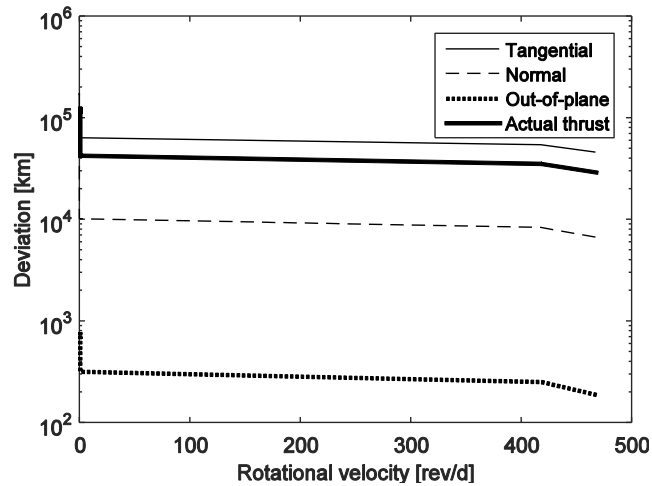
Figure 19. Deviation of the asteroid at the check point as function of the initial rotational velocity of the asteroid.

8   Conclusions

This paper presented a strategy to simultaneously deflect the trajectory of an asteroid and control its rotational motion via laser ablation. In order to maintain the optimal focussing of the laser, a precise guidance, navigation and control system was implemented to control the position of the spacecraft within a limit sphere at a given distance from the asteroid. Camera and ranging instruments were used to estimate the spacecraft relative motion, while additional information from an impact sensor was used to separate the plume impingement contribution from the actual acceleration due to the laser ablation. In this way, it was possible to accurately estimate the deflection action on the asteroid without relying on any interaction model between the laser and the asteroid.

The paper demonstrates that laser ablation can be employed to reduce the angular velocity of the asteroid by pointing the laser off-barycentre. It was shown that, if an initial map of the asteroid and estimation of its attitude and centre of mass are available, it is possible to decrease the asteroid's spin rate in few days of operations with a moderate size laser. It was demonstrated that the control of the rotation can significantly improve the deflection action for the same total mass into space.

9   Acknowledgments

10 References

Anisimov, S. I., Khokhlov, V. A.: 1995, 'Instabilities in laser-matter interaction'. **CRC press**. Boca Raton, FL.

Chapman C. R. and Morrison D.: 1994, 'Impacts on the Earth by Asteroids and Comets: Assessing the Hazard', **Nature**, Vol. 367, No. 6458, Jan. 1994, pp. 33–40, doi: 10.1038/367033a0

Colombo, C., Sanchez Cuartielles, J. P., Vasile, M., Radice, G.: 2006, 'A comparative assessment of different deviation strategies for dangerous NEO'. IAC-06-A3.P.05, **57ᵗʰ International Astronautical Congress**, October 2 – 6, 2006, Valencia, Spain.

Colombo C., Vasile M. and Radice G.: 2009, 'Semi-Analytical Solution for the Optimal Low-Thrust Deflection of Near Earth Objects', **Journal of Guidance, Control and Dynamics**, Vol. 32, No. 3, May–June 2009, pp. 796–809, doi: 10.2514/1.40363.

Crassidis, J.L., and Junkins, J.L.: 2004, Optimal Estimation of Dynamic Systems, 1st Edition, **Chapman & Hall/CRC Press**, Boca Raton, FL.

Dionne, K.: 2009, 'Improving Autonomous Optical Navigation for Small Body Exploration Using Range Measurements'. AIAA 2009-6106. **AIAA Guidance, Navigation, and Control Conference**, 10 - 13 August 2009, Chicago, Illinois, USA.

Dhome, M., Richetin, M., Lapreste, J.T., Rives, G.: 1989, 'Determination of the Attitude of 3-D Objects from a Single Perspective View'. IEEE Transactions on pattern analysis and machine intelligence. Vol II. No. 12. December 1989.

Gibbings, A., Vasile, M., Watson, I., Hopkins, J.-M., and Burns, D. (2013) Experimental analysis of laser ablated plumes for asteroid deflection and exploitation. **Acta Astronautica**, 90(1), pp. 85-97. (doi:10.1016/j.actaastro.2012.07.008).

Hashimoto, T., Kubota, T., Mizuno, T.: 2003, 'Light weight sensors for the autonomous asteroid landing of MUSES-C mission'. **Acta Astronautica**, Volume 52, Issues 2–6, January–March 2003, Pages 381–388.

Hu, W. and Scheeres, D. J.: 2002, 'Spacecraft motion about slowly rotating asteroids'. **Journal of Guidance, Control and Dynamics** 25 (4), 765–775.

Johnson, A.E. and Matthies, L. H.: 1999, 'Precise Image-Based Motion Estimation for Autonomous Small Body Exploration'. In: **5th International Symposium on Artificial Intelligence, Robotics and Automation in Space** (iSAIRAS'99), pp. 627-634.

Lagarias, J.C., Reeds, J. A., Wright, M. H. and Wright, P. E.: 1998, 'Convergence Properties of the Nelder-Mead Simplex Method in Low Dimensions'. **SIAM Journal of Optimization**, Vol. 9 Number 1, pp. 112-147, 1998.

Longuet-Higgins, H.C. and Prazdny, K.: 1980, 'The interpretation of a moving retinal image'. **Proceedings of the Royal Society of London** B 208, 385-397.

Maybeck, Peter S.: 1979, 'Stochastic Models, Estimation, and Control'. **Mathematics in Science and Engineering**. 141-1. New York: Academic Press. pp. 423. ISBN 0-12-480701-1.

Nister, D.: 2006, 'An Efficient Solution to the Five-Point Relative Pose Problem'. **IEEE Transactions on pattern analysis and machine intelligence**. Vol 26. No. 6. June 2006.

Noda H., Mizuno T., Kunimori H., Takeuchi H., Namiki N.: 2013, 'Alignment measurement with optical transponder system of Hayabusa-2 LIDAR'. In:Proceedings of **Eighteenth International Workshop on Laser Ranging Instrumentation.**

Sanchez J. P., Colombo C., Vasile M. and Radice G.: 2009, 'Multi-Criteria Comparison among Several Mitigation Strategies for Dangerous Near Earth Objects', **Journal of Guidance, Control and Dynamics**, Vol. 32, No. 1, Jan.-Feb. 2009, pp. 121-142, doi: 10.2514/1.36774.

Schaub, H., Junkins, J. L.: 2003. 'Analytical mechanics of space systems', 1st Edition. **AIAA Education Series.** AIAA, Virginia, U.S.A.

Seboldt W., Reichert M., Hanowski N. and Novara M.: 2000, 'A Review of the Long-Term Options for Space Exploration and Utilisation', **ESA Bulletin**, Vol. 101, Feb. 2000.

Siegman, A. E.: 1986, 'Lasers'. **University Science Books**. 55D Gate Five Road, Sausalito, CA. pp. 664–669. ISBN 0-935702-11-3.

Thiry, N and Vasile, M 2014, 'Recent advances in laser ablation modelling for asteroid deflection methods'. in EW Taylor & DA Cardimona (eds), **Proceedings of SPIE** - The International Society for Optical Engineering: Nanophotonics, Macrophotonics for Space Environments VIII. Vol. 9226, 922608, San Diego, California, 8th Nanophotonics and Macrophotonics for Space Environment Conference, NMSE 2014, San Diego, United Kingdom, 18-19 August., 10.1117/12.2060810.

Thiry, N and Vasile, M 2015, 'Impact of the Tumbling Rate on the Performance of a CW Laser Deflection System for Asteroids', **4th IAA Planetary Defense Conference**, 13-17 April 2015, ESA-ESRIN Frascati, Italy.

Vasile M., Colombo C.: 2008, 'Optimal Impact Strategies for Asteroid Deflection'. **Journal of Guidance, Control, and Dynamics**, Vol. 31, No. 4, July–August 2008, pp. 858–872, doi: 10.2514/1.33432.

Vasile M., Maddock C.: 2012, 'Design of a Formation of Solar Pumped Lasers for Asteroid Deflection', **Advances in Space Research**, Vol. 50, No. 7, 01.10.2012, p. 891-905.

Vasile M., Vetrisano M., Gibbings A., Garcia Yarnoz D., Sanchez Cuartielles J-P., Burns D., Hopkins J-M., Colombo C., Branco J., Wayman A., Eckersley S.: 2013, 'Light Touch[2], Effective Solutions to Asteroid Manipulation', **ESA Final report, SysNova Study**, ESA Reference Nos.: 12/X02, 12/X03, February 2013.

Vasile M., Vetrisano M., Gibbings A., Garcia Yarnoz D., Sanchez Cuartielles J-P., Hopkins J-M., Burns D., McInnes C., Colombo C., Branco C., Wayman A., Eckersley S.: 2013b, 'Light-Touch[2]:2013, A Laser-Based Solution for the Deflection, Manipulation and Exploitation of Small Asteroids', **Planetary Defense Conference 2013**, Flagstaff, USA, IAA-PDC13-04-22.

Vasile, M., Gibbings, A., Watson, I., Hopkins, J.-M., 2014. Improved laser ablation model for asteroid detection. **Acta Astronautica 103**, Acta Astronautica, 103. pp. 382-394. ISSN 0094-5765.